Ana de Melo Samouco

Bachelor Degree in Sciences of Physics Engineering

Laser induced electrodes towards low cost flexible electronics and its applications in a UV sensor

Dissertation submitted in partial fulfillment
of the requirements for the degree of

Master of Science in
Physics Engineering

Adviser: Prof. Dr Elvira Maria Correia Fortunato, Full Professor,
NOVA University of Lisbon

FACULDADE DE
CIÊNCIAS E TECNOLOGIA
UNIVERSIDADE NOVA DE LISBOA

September, 2017

Laser induced electrodes towards low cost flexible electronics and its applications in a UV sensor

Copyright © Ana de Melo Samouco, Faculdade de Ciências e Tecnologia, Universidade NOVA de Lisboa.
A Faculty of Sciences and Technology e a NOVA University of Lisbon têm o direito, perpétuo e sem limites geográficos, de arquivar e publicar esta dissertação através de exemplares impressos reproduzidos em papel ou de forma digital, ou por qualquer outro meio conhecido ou que venha a ser inventado, e de a divulgar através de repositórios científicos e de admitir a sua cópia e distribuição com objetivos educacionais ou de investigação, não comerciais, desde que seja dado crédito ao autor e editor.

This document was created using the (pdf)LaTeX processor, based in the "novathesis" template[1], developed at the Dep. Informática of FCT-NOVA [2].
[1] https://github.com/joaomlourenco/novathesis [2] http://www.di.fct.unl.pt

Eles não sabem, nem sonham,
que o sonho comanda a vida,
que sempre que um Homem sonha
o mundo pula e avança
como bola colorida
entre as mãos de uma criança.
Rómulo de Carvalho em Pedra Filosofal

Acknowledgements

Completo agora mais uma etapa da minha vida pessoal e profissional, com um enorme sentimento de realização por tudo aquilo que aprendi, cresci e vivi. Foram muitos os que me ajudaram e apoiaram a percorrer esta jornada e a quem agradeço profundamente.

À minha orientadora, professora Elvira Fortunato, por todas as condições de trabalho que proporcionou, pela sua orientação, preocupação, interesse e confiança.

À Carolina Marques, pelo constante apoio, disponibilidade e amizade que demonstrou. Pela sua boa disposição, e positivismo que tanto me motivou, por todos os conhecimentos que me transmitiu e por todas as pausas, risos e desabafos.

À Ana Pimentel, pela sua ajuda fundamental com as sínteses de óxido de zinco e caracterizações dos sensores. Por todas as opiniões e respostas dadas, pela sua amizade.

A todos os que me ajudaram nas caracterizações das minhas amostras, em particular à Sónia Pereira e Joana Pinto pelo cuidado e tempo que disponibilizaram na técnica de analise de Difração de raios-X. À Daniela Gomes pelas imagens das minhas amostras obtidas no microscópio eletrónico de varrimento. À Maria João pelos espectros de Raman.

À Alexandra Gonçalves por todo o auxílio que me deu no laboratório e por todas as respostas aos meus pedidos. À Raquel Borda d'Água e à Sofia Ferreira pelo constante à vontade que sentia sempre que lhes invadi o espaço.

Aos meus colegas de laboratório pelo ambiente de trabalho sempre descontraído e bem disposto. Ao pessoal do *open space* pela integração, e por todos os momentos *after work* proporcionados. Aos meus colegas de curso, por, mesmo que mais distantes nunca termos perdido o contacto.

Ao T'Salvador pela ideia da engenhoca, e aos meus avós pelo permanente apoio, orgulho e exemplo mostrado que tantas forças me deram.

À minha tia, por todas as marmitas feitas com tanto carinho, por toda a preocupação e por sempre proporcionar o melhor ambiente de trabalho.

Aos meus pais, por me terem proporcionado esta aventura, por sempre me segurarem por mais que vos custasse e por nunca me cortarem as asas. Aos meus irmãos, Simão e André, pelas constantes mensagens de apoio e por serem quem são.

Ao Ricardo Adão, pela maravilhosa amizade, por todas as deslumbrantes aventuras e por sempre me apoiares e ajudares sem nunca me deixares desistir. Sem ti seria tudo mais difícil.

Benjamin Zander uma vez disse, *Sucesso não está relacionado com riqueza, poder e*

fama, mas sim com a quantidade de olhos brilhantes que temos à nossa volta. E todos vocês brilharam com os meus. Um grande grande obrigada.

Abstract

Flexible electronics is a branch of electric fabrication that allows increasingly smaller and ergonomic devices. However, its production is still a multi-step process, expensive and time consuming.

Laser direct writing (LDW) is a clean and low cost alternative technique to produce electrodes on flexible substrates that allows high resolution, without the need of masks or direct contact of the system with the device. Moreover, to produce graphene based flexible devices is required the use of expensive techniques, controlled environments and long production times. Laser induced graphene (LIG) emerges thus as a rising substitute to produce such devices. LIG has as an essential feature the CO_2 infrared laser locally irradiation of polyimide (PI) or polyetherimide (PEI) films where the product is mainly graphene stacked structures.

This work consisted in the development and optimization of flexible UV sensors that uses zinc oxide nanorods as the active layer for the detection, PI or PEI as the substrates and its respective LIG as electrodes. The nanorods with higher area-volume ratio, synthesized through a microwave assisted hydrothermal method, were selected and deposited by drop casting onto the electrodes that in turn were optimized to enhance electrical properties by varying the laser parameters.

The assembled sensors were able to successfully detect the UV radiation with a responsivity of 92 and 2 nA/W for 1 V bias for the PI and PEI substrates, respectively. In addition the PI sensor shown to be capable of working under strain and to be stable after several hours of constant operation.

Moreover to complement the LDW study it was produced laser induced silver and copper electrodes on paper subtracts with promising but still preliminary outcomes.

Keywords: Laser direct writing, Laser induced graphene, Graphene stacked structures, Zinc oxide nanorods, UV sensor, flexible electronics.

Resumo

Eletrónica flexível é um ramo da fabricação elétrica que permite ter dispositivos cada vez mais pequenos e ergonómicos. No entanto, a sua produção ainda envolve vários passos, é dispendiosa e demorada.

Escrita direta por laser é uma técnica alternativa limpa e de baixo custo para produzir elétrodos em substratos flexíveis que permite alta resolução, sem utilização de máscaras, ou de contacto direto com as amostras. Especialmente para produzir elétrodos flexíveis tendo como base grafeno, onde é necessário o uso de técnicas dispendiosas, ambientes controlados e longos tempos de produção. Grafeno induzido por laser (GIL) emerge assim como um substituto em ascensão para produzir tais dispositivos. GIL tem como principal característica a irradiação localizada de folhas de poliimida (PI) e polieterimida (PEI) por laser infravermelho de CO_2 onde o produto é principalmente estruturas empilhadas de grafeno.

Este trabalho consistiu no desenvolvimento e otimização de sensores de radiação ultravioleta (UV) que usa nanoestruturas de oxido de zinco como a camada ativa para a deteção, PI e PEI como substratos e os respetivos GIL como elétrodos. As nanoestruturas com uma maior razão de área-volume, sintetizadas por um método hidrotermal assistido por micro-ondas, foram selecionadas e depositadas por *drop casting* em cima dos elétrodos que por sua vez foram também otimizados variando as condições do laser de modo a melhorar as suas propriedades elétricas.

Os sensores produzidos detetaram com sucesso a radiação ultravioleta com uma responsividade de 92 e 2 nA/W para uma tensão de 1V nos substratos de PI e PEI respetivamente. Para além disso o sensor PI mostrou ser capaz de trabalhar quando mecanicamente deformado e após várias horas de constante funcionamento.

Ademais, para completar o estudo sobre escrita direta por laser, foram produzidos elétrodos de prata e cobre induzidos por laser em substratos de papel com resultados promissores, mas ainda preliminares.

Palavras-chave: Escrita direta por laser, Grafeno induzido por laser, grafeno poroso, nanoestruturas de oxido de zinco, sensor UV, Electrónica flexível.

Contents

List of Figures

List of Tables

Acronyms

CB	Conduction Band.
CENIMAT	Centre for Materials Research.
DI water	Deionized water.
EDS	Energy Dispersive Spectroscopy.
LDW	Laser Direct Writing.
LDW-	Laser Direct Writing Subtraction.
LDW+	Laser Direct Writing Addition.
LDWM	Laser Direct Writing Modification.
LED	Light-Emitting Diode.
LIG	Laser Induced Graphene.
PEI	Polyetherimide.
PI	Polyimide.
PPI	Pulses Per Inches.
RGB	Red, Green and Blue.
SE	Secondary Electrons.
SEM	Scanning Electron Microscopy.
ULS	Universal Laser System.
UNL	Nova University of Lisbon.
UV	Ultraviolet.
VB	Valence Band.

XRD X-Ray diffraction.

Chapter 1

Introduction

1.1 Motivation of the work

In the last few years, flexible electronics devices have been the target of extensive research, mainly due to their wide range of potential daily-life applications. Such devices required the study of new materials that can provide flexible properties. In 2010 the Nobel prize of physics was attributed to Andre K. Geim and Konstantin S. Novoselov for the discovery of graphene - a monolayer of carbons arranged in a hexagonal lattice. Since its discovery, graphene has been the target of extensive scientific research due to its unique electrical, optical and mechanical properties.

Nowadays, the techniques used for the production of graphene and graphene-like materials typically require expensive equipment, high temperatures or several steps of chemical synthesis. However, a low-cost technique for production of porous graphene has recently been implemented. The technique is known by Laser Induced Graphene (LIG) and it consists on the irradiation of a polymer surface with pulsed CO_2 infrared laser light, to promote a chemical reaction whose product is mainly graphene stacked-structures. Hence, LIG emerges a promising alternative for the production of low-cost flexible devices, including a wide range of sensors.

As a consequence of the depletion of the ozone layer in earth's atmosphere during the last few decades, the surface levels of UV radiation has increased drastically, leading to countless harmful consequences for life on earth. Thus, devices capable of detecting UV light are gaining more and more attention, specially those composed with non toxic and stable materials.

1.2 Objectives

In this work it is proposed the development of a low-cost UV sensor on a flexible substrate according to the following steps:

1. Production and optimization of graphene-like electrodes with a CO_2 infrared cutting laser;
2. Synthesis of zinc oxide nanoparticles using a low-cost and energy efficiency method;
3. Implementation and characterization of an UV sensor through the combination of the previous steps.

Chapter 2

Concepts and physical principles

2.1 Flexible Electronic

The advance of technology has allowed the society to get closer and closer to its whims and needs mainly due to the possibility of manufacturing increasingly smaller and ergonomic devices. Flexible electronics is a branch of electric fabrication that is in part responsible for these improvements.

An electronic device is considered flexible when it is able to bend in several directions without losing its electrical properties [1]. These mechanical properties open up new kinds of applications for electronic such as strides in bendable transistors [2] and opto-electronic devices [3], paper electronics [4], smart clothing and electronic textiles [5] but also in the medical field such as conformable skin sensors [6], smart surgical gloves[7], and structural health monitoring devices [8] (figure 2.1).

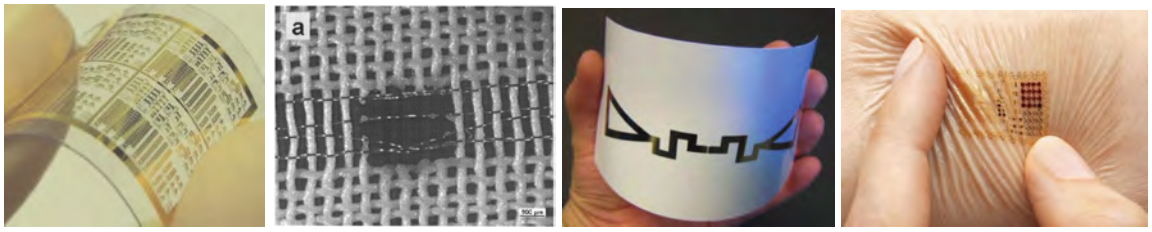

a b c d

Figure 2.1: Flexible electronics a) Carbon nanotube thin-film transistors and integrated circuits on a flexible and transparent substrate [9], b) Interconnect experiments performed on a woven test ribbon [5], c) A printed, passive radio-frequency identification gas sensor node on paper [4], d) Skin sensor [10].

There are two possible ways to achieve flexible electronics. The first one relates to

introducing flexible and stretchable properties in naturally rigid structures (e.g. semiconductors). The second relates to materials that are intrinsically bendable (e.g. organic materials) and implementing them on electrical circuits. However both approaches are far from perfection. On the one hand, the electrical properties of the organic materials are relatively poor compared to that of inorganic materials, which lead to low efficiency organic devices [11]. On the other hand, the crystalline structure of semiconductors confer them strong rigidity, which makes them nearly impossible to stretch.

The selection of electrodes to be used in flexible electronics is also of utmost importance, especially when it comes to their electrical characteristics and adaptability to flexible substrates [12].

The compliant electrodes should have a low electrical resistance for faster and more efficient devices. Lower resistance minimizes the time constant RC and the power consumption I^2R respectively, where R is electrical resistance (Ω), C is the circuit capacitance (F) and I the electrical current (A). The electrical resistance is given by equation 2.1, where ρ refers to the bulk resistivity (Ω·m) and l, t and ω refer to the length, the thickness and the width of the electrode, respectively.

$$R = \frac{\rho}{t}\frac{l}{\omega} \tag{2.1}$$

However, because accurately measuring the thickness t of thin conductive films can many times prove to be quite challenging, when mentioning flexible conductors, the sheet resistance R_s (equation 2.2) is often used as the electrical characteristic of the electrode, in replacement of the electrical resistance R.

$$R_s = \frac{\rho}{t} \tag{2.2}$$

Nonetheless, the electrical characteristics of the compliant electrodes are not the only parameters to be taken into account. A flexible electrode must yield strong adhesion to the substrate and a low mechanical impedance to deformation, so that it can be the substrate to restrict the strain and not the electrode [12].

Taking into account the above statements, flexible electronics still have a lot of optimization work ahead and the search and development of new alternatives is in constant progress.

In 2010, the Nobel Prize in Physics committee honored two scientists, Andre K. Geim and Konstantin S. Novoselov from the University of Manchester UK (figure 2.2a), for producing, isolating, identifying and characterizing a monolayer of carbon packed in a hexagonal lattice, with a carbon-carbon distance of 0.142 nm - to this structure is given the name of graphene(figure 2.2b) [13].

Since the proof of concept of graphene, extensive research has been performed on the topic, mainly due to its outstanding mechanical, electrical and optical properties and the broad applicability in flexible electronics [14]. Graphene is extremely thin (one atom thick), mechanically extremely strong (substantially stronger than steel), highly

stretchable and nearly transparent. Its electrical conductivity is extremely high, with the possibility of further increase trough chemical doping [15].

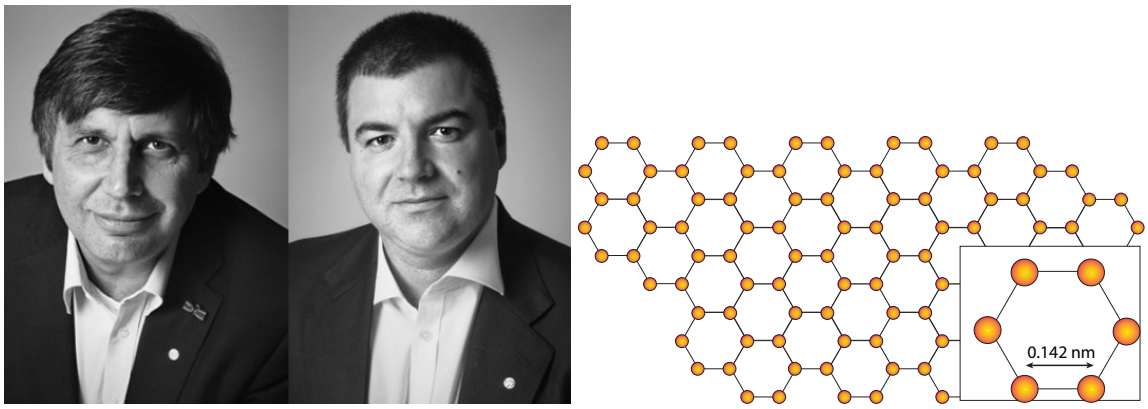

a b

Figure 2.2: Graphene: (a) Andre K. Geim and Konstantin S. Novoselov, awarded of the Nobel Prize in Physics 2010, (b) Atomic structure of graphene.

Graphene-like structures, with similar characteristics to graphene now arise as alternatives to the absolute monolayer graphene. For instance porous graphene also exhibits high conductivity and a high surface area, which may be advantageous for sensors in surface-sensitivity enhanced devices due to its 3-dimensional structure [14].

2.2 Laser Direct Writing

Nowadays, implementing materials onto flexible substrates is typically performed by printing techniques such as screen-printing, inkjet-printing or slow-flow assisted assembly. However, these processes require several fabrication steps, which makes them time-consuming and significantly costly in fabrication [16]. Another example is the production of porous graphene with resource to high temperatures or several steps of chemical synthesis [17].

The scientific community has been trying to achieve alternatives to the conventional procedures in order to improve them. So far, Laser Direct Writing (LDW) arises as one of the most promising methods for obtaining electrodes in flexible substrates, for it enables high resolution, rapid fabrication and wide freedom of design. It does not require the use of masks, neither complex clean-room environment, and yields considerably a lower costs than its alternative technique.

LDW enables the implementation patterns on a material surface either in a series mode or in a laser-beam "spot-by-spot"configuration. In the latter, a robotics system is controlled by a computer software, which enables the precise control and high resolution of the patterning, without the need of masks, nor the direct contact between the system and the substrate [18]:

1. By a photochemical, photothermal or photophysical process, it can remove material of the substrate resulting in laser scribe, cutting, drilling or etching - Laser Direct Writing Subtraction (LDW-);

2. It can add material to the substrate, using various laser-induced processes - Laser Direct Writing Addition (LDW+);

3. Or the laser beam can promote permanent structural or chemical changes in the material, due to photochemical or photothermal processes, which are not enough to produce ablative effects in the substrate - Laser Direct Writing Modification (LDWM).

Laser cutting systems are extensively used in industry with a wide range of powers and wavelengths. It is possible to use this type of laser to produce electrodes in flexible substrates by laser direct writing technology, in particular LDWM, and implement it in the industry with a decrease in cost and an increase in repetition rates.

In the literature there is already reports on the production of conductive materials in flexible substrates through the LDW technique, for example copper [19, 20], silver [16, 21] and porous graphene [17, 22–24].

2.2.1 Laser Induced Graphene

LDW was first used as a means to produce graphene-based electrodes, when a laser beam was able to reduce graphene oxide, figure 2.4. Once the reproducibility of this process was verified, several electronic devices were produced using this technique for example, in sensors of strain, gas and humidity, supercapacitors, transistors and photodetectors [25].

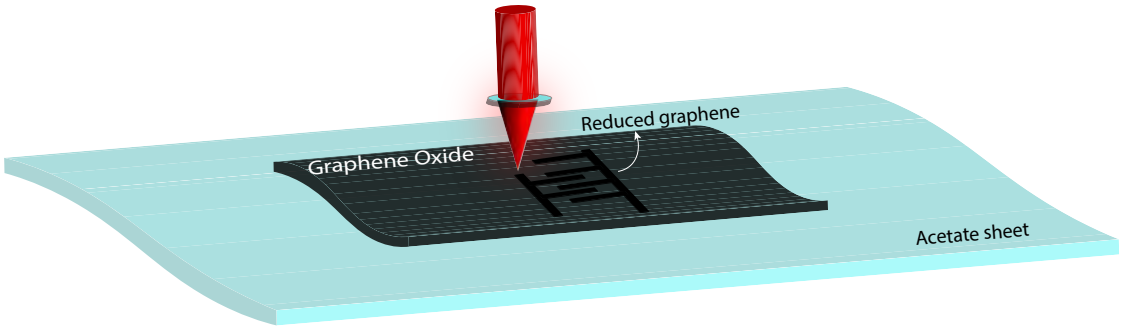

Figure 2.3: Schematic of the first graphene-like electrodes produced using laser direct writing technique.

Polyimide (PI) is a type of polymer known for its high heat-resistance and stability with temperatures up to 400 °C [26]. Since its commercialization in 1955, this polymer has been target of several studies in particular, in laser ablation and the effects of exposure to laser irradiation. In 1989, long before the discovery of graphene, it was reported that an ablated area of PI became carbonized and yielded a conductivity increase up to

twelve orders of magnitude, therefore allowing the patterning of conducting paths in still insulating matrices [27]. After this findings, several other research groups studies this phenomenon using pulsed UV laser sources, with the main purpose of probing the products of the laser ablation process [28–30].

In 2014, Lin et al. [17] used a commercial CO_2 infrared laser-cutting system to irradiate the surface of this polymer and fully characterized the carbonaceous product of the irradiation. For the first time, the results were correlated to the presence of graphene stacked structures, with an optimized sheet-resistance of 15 $\Omega/square$. To this technique was given the name of Laser Induced Graphene (LIG). Furthermore, this group also found potential applicability for flexible electronics.

LIG is formed by a photothermal process: when a laser beam is focused on the polymer surface, thermally induced lattice vibrations lead to extremely high localized temperatures, which are capable of breaking the C-O, C=O and the N-C bounds. Following, a recombination of the sp^3-carbon atoms (aromatic compounds) into sp^2-carbon atoms (graphitic structures) [17] and the other elements are released in form of gases (CO, CO_2, HCN, and C_2H_2 [30]). A representation of the reaction can be found in Figure 2.4.

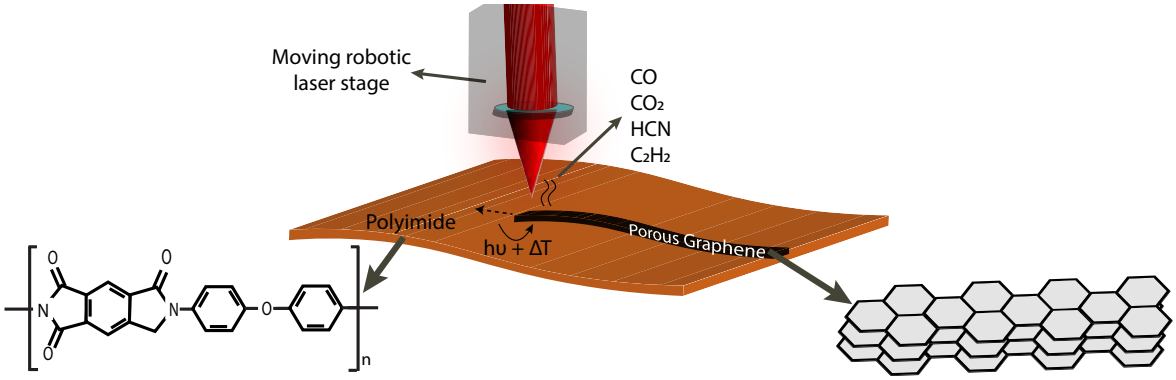

Figure 2.4: Schematic of production of laser induced graphene stacked structures in polymide substrate.

Lin et al. tested fifteen different polymers in order to verify if LIG was a process capable of been generalized. However, out of the fifteen polymers only PI and the Polyetherimide (PEI) showed this effect. The reason why this happened is not yet completely understood, however, PI and PEI were the only polymers which contained aromatic[1] and imide[2] repeat units, emphasizing the importance of the polymers chemical structure to the occurrence of LIG.

Following these findings, several research teams pursued this technique and nowadays it is possible to find a wide range of electrical devices that are based on laser-induced graphene. For example, super capacitors energy storage devices [31–34], stretchable sensors [25, 35] and glucose sensors [36].

[1] Aromatic compounds are substances that consist of one or more rings that contain alternating single and double bounds in its chemical structure.

[2] Imide is a functional group consisting of two acyl groups bound to nitrogen.

2.3 Zinc oxide nanoparticles in UV sensors

Ultraviolet (UV) light is an electromagnetic radiation with a wavelength between 10 nm (124 eV) and 400 nm (3 eV). In the electromagnetic spectrum the UV light lies between the visible and X-ray radiation and it can be split into the subdivisions presented in figure 2.5.

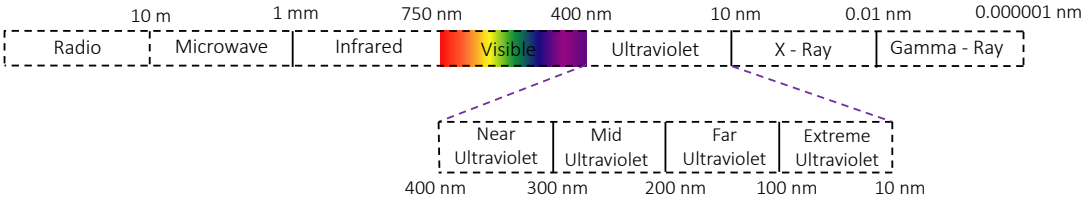

Figure 2.5: Electromagnetic spectrum where it is visible the subdivisions of the ultraviolet light.

Twenty-five percent of the UV light from the Sun reaches the surface of Earth. UV light contributes for the production of vitamin D whose deficiency results in bone fragility in the elderly and has been indirectly connected to heart disease and diabetes. In higher doses however, when in excess, it can cause skin cancer [37]. An equilibrium of UV exposure is required for a healthy lifestyle. With the depletion of the ozone layer increases the surface levels of UV light, leading to countless harmful consequences for life on earth. Thus, devices capable of detecting UV light are gaining more and more attention, specially those composed with non toxic and stable materials.

A sensor is a device that responds to a physical or chemical stimulus by converting it into an interpretable output, usually in the form of an electric signal. A photosensor converts the energy of a photon into electric current and should suit the following requirements[38]:

- High responsivity,
- High signal-to-noise ratio,
- High spectral selectivity,
- High response and recovery time,
- High stability.

The responsivity is determined according to equation 2.3 [39],

$$Responsivity = \frac{I_{ph} - I_{dark}}{P_{UV}} \tag{2.3}$$

where I_ph is the UV sensor photocurrent, I_{dark} is the UV sensor dark current and P_{UV} is the power of the UV source [39]. The signal-to-noise ratio is an indicator of statistical

variation of a measurement to around a signal. Higher signal-to-noise ratios allow distinguishing real defects from noise related artifacts. Spectral selectivity relates to the narrow band-width to which the sensor responds. The response time is the time taken by a sensor to reaches 95% of its stable value, and the recovery time is defined in a similar way to conversely [40]. A high stability refers to a constant signal with few fluctuations.

2.3.1 Zinc Oxide Nanoparticles

Zinc oxide (ZnO) is a n-type semiconductor and it is one of the most used materials in UV sensor devices [41]. At room temperature it has a wide band gap of 3.3 eV, a high excitation energy (60 eV) and a hexagonal wurtzite crystalline structure with the lattice parameters $a = 0.349$ nm and $c = 0.520$ nm. This material has low toxicity, an excelent chemical and thermal stability, a wide range of electrical conductivity (between 10^{-9} and $10^{4}\ \Omega{\cdot}\mathrm{cm}^{-1}$), a big abundance in nature and a low production price [42]. These properties makes ZnO a material to be used in the most varied fields such in film transistors[43], dye sensitized solar cells[44] and photodetectors[45, 46].

As the size of the ZnO particles decreases reaching sizes in the order of nanometers (nanoparticles), the physical and chemical properties of ZnO became strongly dependent on the size, shape and crystallinity of the synthesized nanostructures. For sensoring applications, it is important to have a high surface-to-volume ratio turning the nanoparticles with a high sensitivity to ambient conditions[47].

Several ZnO synthesis techniques were already tested and they can be divided into three main types, chemical, biological and physical synthesis. Depending on the process behind the synthesis, these three types can be split into different methods, and by controling the synthesis parameters process it is possible to control the final properties of the synthesized structures. Table 2.1 summarize the most used processes[48].

Table 2.1: Summary of the major techniques used for ZnO nanoparticles synthesis. Adapted from [48]

ZnO nanoparticles synthesis	**Chemical synthesis**	Gas Phase	Pyrolysis Gas condensation method
		Liquid Phase	Precipitation/coprecipitation method Colloidal method Sol-gel processing Oil microemulsion method Hydrothermal method Solvothermal method
	Physical synthesis	High energy ball milling Solid, physical and chemical vapor deposition Laser ablation	
	Biological synthesis	From waste material Microbes mediated (fungi, algae, bacteria) Plant mediated (roots, shoots, leaves, stem)	

Chemical synthesis is the process that has a more advantageous income and cost ratio. However it is necessary to take into account the factor time and efficiency of the process: the faster and the more energetic efficient the synthesis is the better. Microwave assisted hydrothermal synthesis is one of the most promising techniques once it allows a fast and homogeneous volumetric heating due to the interaction of the electromagnetic waves with the molecules leading to a "molecular heating"instead of the conventional conductive heating with an external heat source that is completely dependent on convection currents and on the thermal conductivity of the various materials that must be penetrated until it reaches the solution[49]. In addition, with microwave assisted hydrothermal synthesis it is possible to have a control on the structure and properties of the synthesis product by adjusting the power inputs, the heating frequency and the time with the possibility to have on/off irradiation cycles [50].

For the chemical synthesis of ZnO it is important to have a reducing agent capable of reduce the respective zinc salt. A frequently used chemical method starts with zinc acetate dihydrate ($Zn(CH_3COO)_2.2H_2O$) dissolved in dionized water and mixed with the reducing agent sodium hydroxide(NaOH) which forms sodium hydroxide which is in turn hydrated and by a heating process forms zinc oxide. The overall reaction can be written as following [51]:

$$Zn(CH_3COO)_2 \cdot 2H_2O + 2NaOH \rightarrow Zn(OH)_2 + 2CH_3COONa + 2H_2O \tag{2.4}$$

$$Zn(OH)_2 + 2H_2O \rightarrow Zn(OH)_4^{2-} + 2H^+ \tag{2.5}$$

$$Zn(OH)_4^{2-} \xrightarrow{heat} ZnO + H_2O + 2OH^- \tag{2.6}$$

2.3.2 UV sensor working principle

The main principle of most semiconductor photodetectors is the internal photoelectric effect. It occurs when a photon is absorbed by a semiconductor resulting in the excitation of an electron from the Valence Band (VB) to the Conduction Band (CB)). Consequently a hole is generated in the VB and a electron-hole pair is created (equation 2.7, squemathic of figure 2.6). The application of an electric field in the material results on the movement of the free charges generating a current in the electrical circuit of the detector[52].

$$hv \rightarrow h^+ + e^- \tag{2.7}$$

However, it was proven that the photoresponse of ZnO nanoparticles is extremely sensitive to the surrounding atmosphere especially at the presence of oxygen molecules [53], meaning that the working principle of a ZnO nanoparticles UV detector is not based solely on the internal photoelectric principle.

In the dark, oxygen molecules tend to be adsorbed on the surface of ZnO nanoparticles as a negative ion captured by free electrons of the semiconductor (equation 2.8). Consequently the depletion layer increases, leading to a reduction of the conductivity once

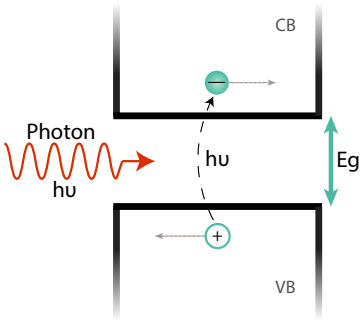

Figure 2.6: Electron-hole photogenerator in a semiconductor.

only the core of the nanoparticles contributes to the conductivity of the device (figure 2.7 on the left).

$$O_2(g) + e^- \rightarrow O_2^-(ad) \tag{2.8}$$

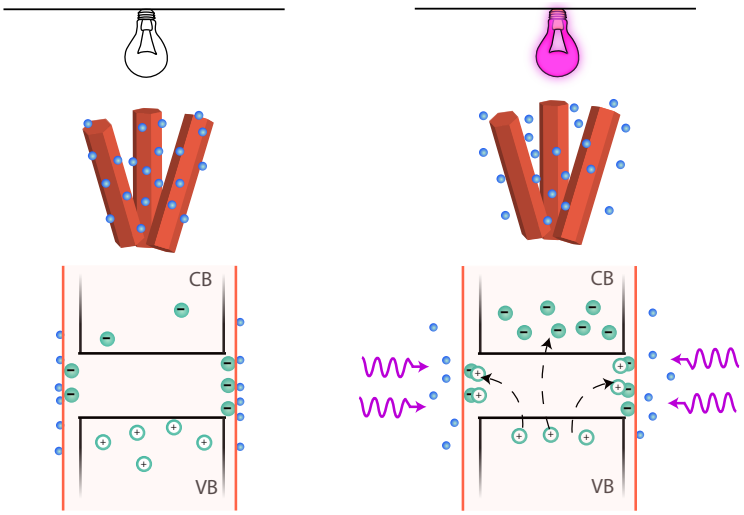

Figure 2.7: Representation of a ZnO nanoparticles photodetector working principle.

When irradiated by an UV photon with energy above the ZnO band-gap the internal photoelectric effect occurs and an electron-hole pair is created. However the holes are rapidly swept to toward the surface and discharge the negative adsorbed oxygen ions (equation 2.9) while the electrons are kept in the inner part.

$$h^+ + O_2^-(ad) \rightarrow O_2(g) \tag{2.9}$$

This particular phenomenon decreases the carrier recombination probability leading to a rise in the photoconductivity (figure 2.7 on the right). After some time it is visible a decay in the conductivity rate due to the desorption of the oxygen by a recombination of the holes with the trapped electrons. These two previous phenomenons (the increase of electrons in the conduction band, and the desorption of the oxygen) favors the oxygen

re-adsorption by attracting the negative charges. It is then a cycle of adsorption and desorption until the equilibrium is reached and the conductivity saturates [38, 53–55].

When the UV light is turned off the photocurrent decays as a result of the trapping of electrons from the conduction band due to the re-adsorption (figure 2.7 on the left) resulting in a decrease of the conductive carriers.

2.4 Fabrication and characterization techniques

This section provides an introduction to the experimental techniques used in the sample fabrication. In particular, the CO_2 laser system used for the LIG, the microwave system used for the nanoparticles synthesis and finally an overview of the characterization techniques.

2.4.1 Commercial CO_2 infrared laser system

Laser is a source of coherent and monochromatic light, derived from the stimulated emission of photons from excited atoms or molecules. The word laser originates from the acronym LASER - Light Amplification by Stimulated Emission of Radiation.

There are three main constituents of a CO_2 laser: (i) a low-pressure laser cavity[3] filled with a gas mixture of carbon dioxide (CO_2), nitrogen (N_2) and helium (He), usually in the volume proportions of 1:5:20, respectively; (ii) an electrical pumping system and (iii) two cavity mirrors placed at each end of the laser cavity, one of which being completely reflective and the other partially transmissive. Figure 2.8 represents a schematic of a CO_2 laser.

In the pumping system, a precise high voltage is applied at the laser cavity for acceleration of electrons and consequent excitation of N_2 molecules by electron collision (figure 2.9). Given the proximity of the N_2 excited state and the upper energy level of CO_2, collisions between excited N_2 and relaxed CO_2 molecules lead to an energy transfer from the former to the latter. Such energy transfer promotes the excitation of CO_2 molecules to their metastable upper state and thereby to inversion of population.

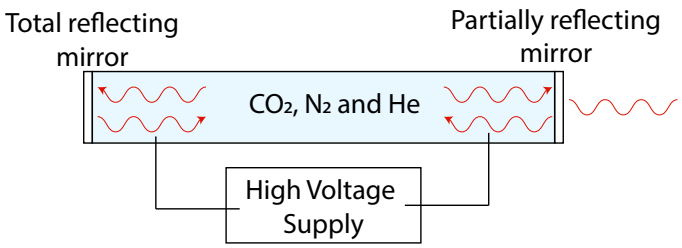

Figure 2.8: Schematic of the main constituents of a CO_2 laser, adapted from [56].

As soon as excited CO_2 molecules spontaneously decay to a partially relaxed energy level, they emit photons which in turn collide with other excited CO_2 molecules.

[3] typically 27 mbar.

In such collisions, because the energy of income photons perfectly matches that of the de-excitation transition, a stimulated relaxation of CO_2 occurs, with the emission of coherent photons, *i.e.* with the same wavelength and phase as the income photons. This phenomenon is called stimulated emission and it is the key for laser emission. The partially relaxed CO_2 molecules are then completely relaxed to the ground state through collisions with He atoms.

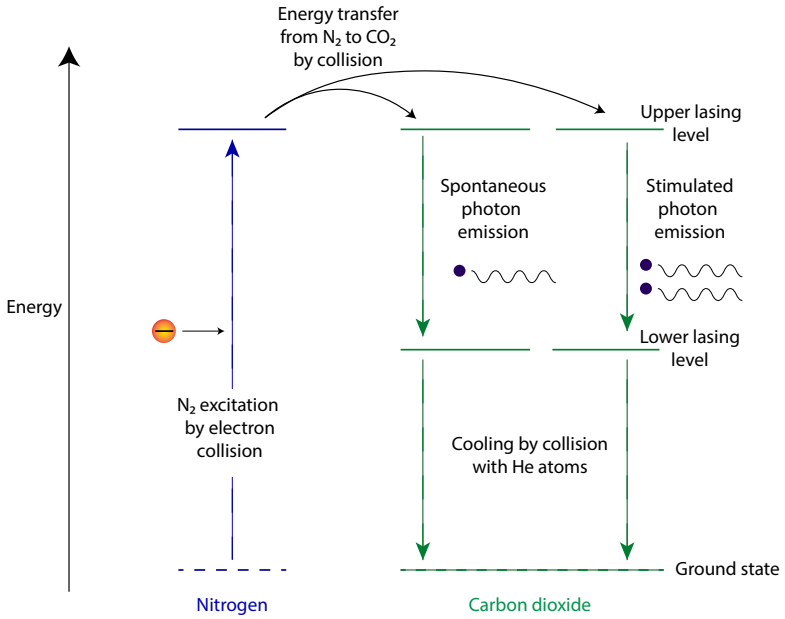

Figure 2.9: The energy spectra of nitrogen (on the left) and CO_2 (on the right) with the several stages envoled for the CO_2 lasing process, adapted from [56].

The amplification of the laser effect is provided by multiple reflections inside the laser resonance cavity, which extends the lifespan of photons inside the gas mixture and results in an avalanche effect of stimulated emissions. At the same time, N_2 molecules continue to be re-energized by electrical pumping thereby transmitting energy to the CO_2 molecules. The output laser beam consists on the fraction of light that is transmitted through the partially reflecting mirror of the resonance cavity [56, 57].

2.4.2 Microwave heating

Microwave radiation consists in electromagnetic waves with a frequency between 300 MHz and 300 GHz and a corresponding wavelength from 1 m to 0.1 cm. In the electromagnetic spectrum, it lies between radio waves and infrared light. It is frequently used in radar devices, satellite communications, food heating or in chemical synthesis.

The heating process is based on the material ability to absorb microwave energy and convert it into heat by an interaction of the electric field either with molecules with a dipole moment (dipolar polarization) or with charged particles (ionic conduction).

In ionic conduction, dissolved charged particles (commonly ions) oscillate with the

alternating electric field of the incident radiation, leading to collisions with neighbor molecules and energy dispersion in the form of heat. In the dipolar polarization, the dipole moments of the molecules tend to align with the applied electric field. However, because the moment realignment is not immediate, a phase shift between the two is generated, leading to energy dampening by molecular friction and collisions and therefore to dielectric heating [49] (figure 2.10a).

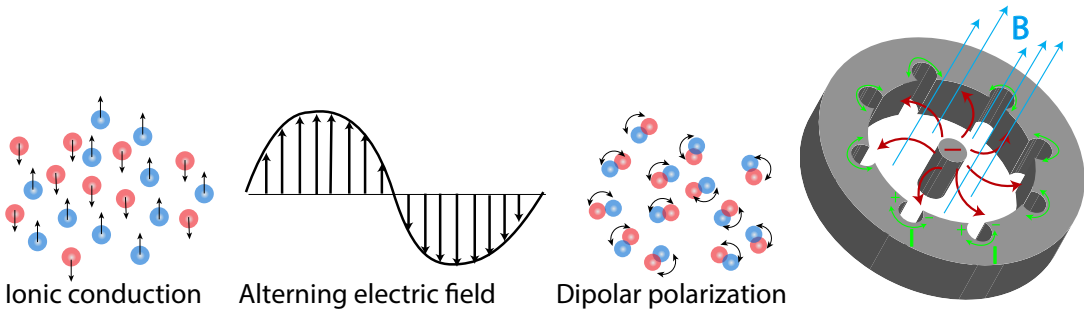

Figure 2.10: Microwave heating a) Schematic of the molecular heating both for ionic conduction and dipolar polarization, b) Schematic of a magnetron where microwave irradiation is formed.

Microwave radiation is produced using three main components (i) a magnetron, the microwave radiation source (ii) a waveguide, responsible to transport the radiation to the target and (iii) the applicator, the target of the electromagnetic radiation. A magnetron consists in a copper tube (anode) with a copper rod inside (cathode) and vacuum between them. When a high voltage is applied across the two conductors, a strong electric field causes loosely bound valence electrons from the copper rod to be removed and accelerated towards the anode. Then, an external magnetic field perpendicular to the electric field is generated by magnets located at the edges of the system in order to deflect the trajectory of the electrons to a spiral motion around the cathode before, as they approach the anode. In turn, the inner surface of the anode copper tube is covered with mall resonant cavities. When the electrons reach the anode, charge displacements are generated at the surface free-charges of the cavities, inducing an oscillation with frequency that is characteristic of the cavity's dimensions. It is due to this oscillations that the microwave radiation are generated [58], figure 2.10b.

The usage of microwave radiation for chemical processes requires precise control of the amount of energy as well as a uniform distribution of radiation through the sample. Large microwave ovens allow the processing of multiple samples simultaneously and containers with different sizes and shapes. However, the larger the oven, the more reflections inside the chamber are likely to form interference patterns, which may lead to uneven distribution of the electric field (multi-mode). This effect may therefore cause positioning-dependent heterogeneity in the heat distribution in the sample, which compromise the

reproducibility of the results. Advances in technology allowed the development of alternative single-mode systems where the radiation is guided directly into the sample without reflections in the path or cavity. This can be obtained through rectangular or circular wave guides, which allow a more precise control of the synthesis conditions (figure 2.11) [59].

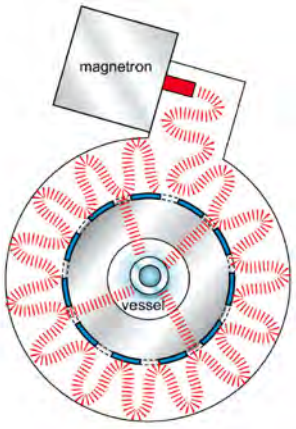

Figure 2.11: Schematic a single-mode microwave applicator [59].

2.4.3 Characterization techniques

The characterization of materials is an important step for retrieving information regarding their structure, composition and other properties. This chapter presents the characterization techniques used in this project and an introduction to their physical principles.

2.4.3.1 X-ray diffraction

XRD is a crystallographic technique which enables analyzing the structural properties of materials. The physical principle behind this characterization technique consists first in the production of the X-ray light and then in the interference of the light with the crystal planes of the sample.

X-rays are mainly generated as a consequence of two major interactions of light and matter, which is typically obtained by the acceleration of electrons towards a metallic target (anode) (figure 2.12). Upon collision with the anode, an electron is removed from the inner electronic shell of an atom, whose vacancy is quickly filled with an electron from a higher shell, whose transition leads to emission of a photon with an energy given by the difference between the two energy levels. Such photons are typically known by characteristic X-rays, for they reproduce the electronic structure of the anode. An alternative interaction is the emission of X-rays due to the sudden deceleration of the primary electrons upon collisions with the electron clouds of the anode. Such emissions of X-rays are called *brehmsstrahlung* and they exhibit a continuous spectrum of energy. For application in XRD, the characteristic X-rays can be isolated using monochromators.

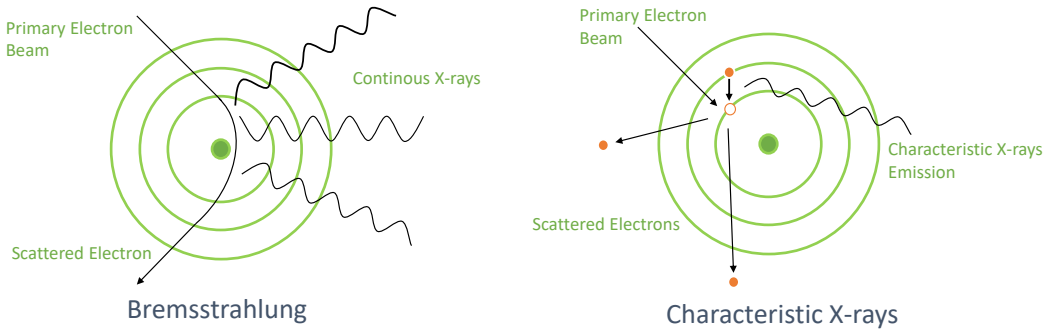

Figure 2.12: Schematic of the two different phenomenons of X-rays generation.

When a sample is irradiated with X-Rays, elastic scattering with the periodic arrays of the material crystalline lattice leads to angle-dependent constructive or destructive interference patterns, which are characteristic of the crystalline structure of the material and can be used for finger-printing. This phenomenon is described by the Bragg's Law (equation 2.10, figure 2.13),

$$n\lambda = 2d_{hkl}sin(\theta) \tag{2.10}$$

where n is an integer number and corresponds to the diffraction order, λ is the wavelength of the incident irradiation, d the interplanar distance, and θ the angle formed between the atomic plans and the x-ray incident beam (and diffracted).

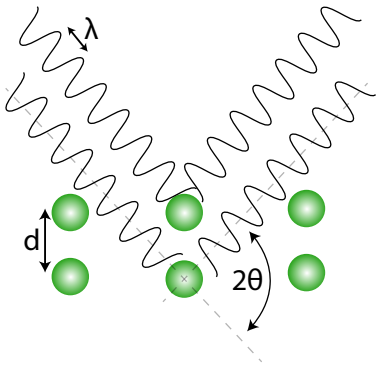

Figure 2.13: Representation of the scattered X-ray light in a crystalline substrate.

A diffractogram is a plot of the diffracted beam intensity as function of the angle θ, where constructive interference appear as peaks. The shape of the diffractogram can be calculated based on the crystal structure of the material or compared to standard reference measurements (retrievable from numerous official databases).

2.4.3.2 Scanning Electron Microscopy

Scanning Electron Microscopy (SEM) consists on focusing an electron beam (0.5 to 30 keV) onto a sample, and measuring the emission of secondary electrons as function of the position of the beam to form an image. The number of electrons detected correlates to variations at the surface of the sample, and because electrons have much smaller diffraction limits than visible light, it is possible to obtain high-resolution images with magnifications up to 300 000 times, without loss of distinctness.

2.4.3.3 Energy Dispersive Spectroscopy

Energy Dispersive Spectroscopy (EDS) allows a chemical characterization of the samples and it is usually coupled to SEM setups.

When an electron beam reaches the sample, alongside the emission of secondary electrons (used for SEM, the beam can also ionize the atoms and make them emit X-rays. The emitted photons have a specific energy depending on the elementary composition of the sample, which can be used to map the abundance of certain elements within the sample.

2.4.3.4 Raman Spectroscopy

Raman spectroscopy is a characterization technique that provides chemical information of a sample through the interaction of light with the analyte.

Monochromatic light, usually from a laser source, is focused on a sample to produce either an elastic (Rayleigh) scattering, if the scattered light has the same frequency as the incident light, or inelastic scattering if otherwise (figure 2.14). Inelastic scattering occurs (i) when the incident light excites a molecule to a higher vibrational level, and then rather than returning to its initial level, it decays to a level of slightly higher energy. Such case is called the Stokes scattering, and the scattered photons contain lower energy than that of the incident photon. (ii) If an already excited molecule is further excited, and then returns to the ground level, then the energy of the scattered photon contains higher energy than that of the incident photon, leading to Anti-Stokes scattering.

The difference between incident and scattered light corresponds to the energy difference between initial and final vibrational levels, which are characteristic of the excited molecule. Raman spectroscopy can therefore be used as a technique for molecular *fingerprinting* within the material.

2.4.3.5 Contact angle

The interaction between a surface and a given liquid can be studied by measuring the so-called contact angle Θc. It is defined by the angle between a plane tangent to a liquid drop and a plane of the surface (figure 2.15).

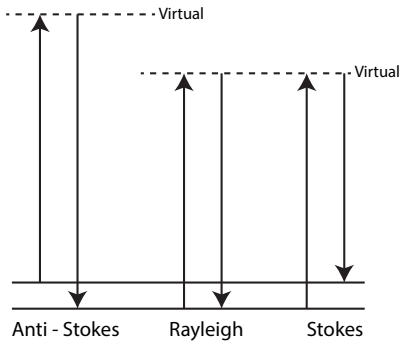

Figure 2.14: Energy level and transitions schematic for Raman and Rayleigh scattering.

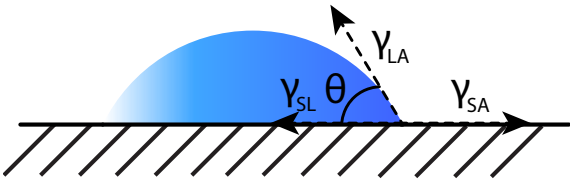

Figure 2.15: Illustrative diagram of the behavior of a drop of liquid on a surface and the contact angle.

The contact angle serves as a quantitative inverse measure of the wettability of a surface [60], which in turn, depends on the thermodynamic equilibrium between the solid, liquid and air interfaces, the adhesive forces between a liquid and solid and finally the cohesive forces within the liquid.

According to the principle of minimum energy, nature always tends to a state of minimum energy. Thus, a liquid spreads on a surface if the energy gained in forming a unit area of solid-liquid interface exceedes the energy requirement to form unit area of the liquid-air interface [61] (equation 2.11),

$$\gamma_{SA} - \gamma_{SL} > \gamma_{LA} \tag{2.11}$$

where γ_{SA}, γ_{SL} and γ_{LA} represent the surface tensions of the solid-vapor, solid-liquid and liquid-vapor interfaces, respectively. In equilibrium, the contact angle Θ between the liquid and the solid surface is given by Young relation, equation 2.12.

$$cos\theta = \frac{\gamma_{SA} - \gamma_{SL}}{\gamma_{LA}} \tag{2.12}$$

The higher the contact angle, the more hydrophobic the surface is. In fact, for contact angles between 0^o and 90^o, the surface becomes wet and is considered hydrophilic, on the other hand, for contact angles between 90^o and 180^o, the substrate is considered hydrophobic.

2.4.3.6 Spectrophotometry

Spectrophotometry is often used to characterize the optical properties of materials. Its working principle consists in the measurement and comparison of the amount of light that is absorbed, reflected or transmitted by a sample with the incident light.

Conventional spectrophotometry devices are composed by five main components: a light source, a monochromator, a sample holder, a detector and a signal converter. The incident light is refracted in the monochromator, which separates its different wavelengths. The split radiation is then cast onto the sample, resulting in wavelength-dependent transmission, absorption and reflection. The fraction of light that reaches the detector is converted into an electrical signal, compared to a measurement of a reference sample and sent to the computer, which in turn measures a spectrum of transmission/absorption as function of the wavelength (figure 2.16).

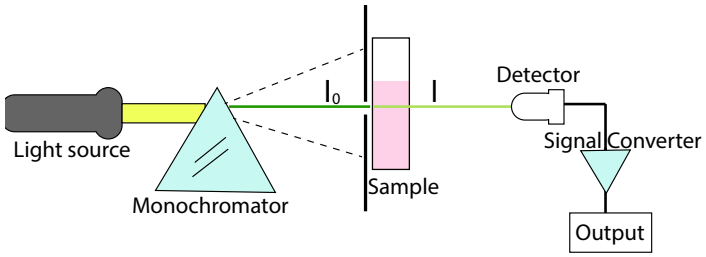

Figure 2.16: Schematic of the spectrophotometer working principle.

The spectrophotometers are divided into two classes, depending on if the sample and reference are measured using a single-beam or a double-beam configuration. In double-beam configuration, the spectrophotometer compares the light intensity between two light paths, one path containing a reference sample and the other the test sample. A single-beam spectrophotometer measures the relative light intensity of the beam before and after a test sample is inserted.

Chapter 3

Materials and Methods

This work is divided in three main parts. The first one consists in the production and optimization of LIG using a CO_2 infrared laser cutting system. In the second part ZnO nanoparticles are synthesized using the microwave assisted hydrothermal technique. The final component of the project involves the assembling of a UV sensor by combining the graphene electrodes produced by LIG and the ZnO nanoparticles.

This chapter begins with a brief description of the equipment used, then it follows by a description of the experimental procedure, in accordance with the previously mentioned components.

3.1 Experimental fabrication and characterization equipment

3.1.1 Commercial CO_2 infrared laser system

The Centre for Materials Research (CENIMAT) at Nova University of Lisbon (UNL) is equipped with an Universal Laser System (ULS) CO_2 VLS 3.5 (figure 3.1a), a pulsed cutting laser (wavelength of 10.6 μm), associated with a plano-convex lens (focal length of 50.8 mm, spot size of 0.127 mm - figure 3.1b). The equipment is designed to operate like a computer printer with a vectorial image input[1], with a computer interface for the encoding of specific laser power, repetition rate and speed parameters in the form of a Red, Green and Blue (RGB) color map.

The laser interface allows defining all laser parameters. The three main variables are the laser power, the speed and the number of PPI. The average laser power (0.05 to 50 Watts), is defined by the duty cycle of the pulses, where the maximum duration (for a 100% of laser power) corresponds to 125 microseconds. The speed determines linear velocity of the laser beam, ranging from 0.00127 to 1.27 m/s. The PPI defines the number

[1] In this work, Adobe Illustrator was used as design software for all printed structures

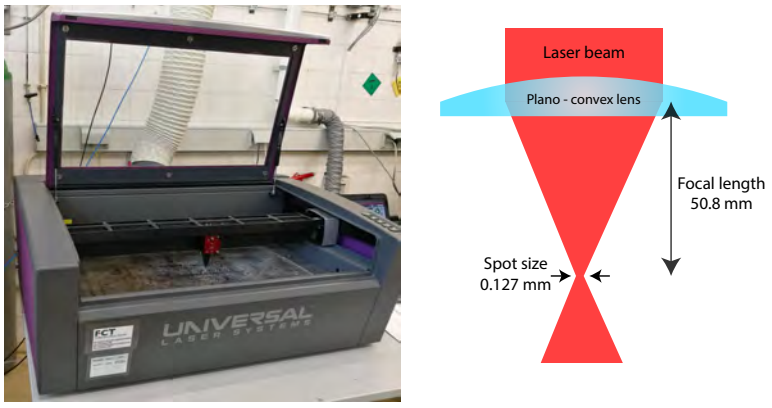

a b

Figure 3.1: Universal Laser System CO2 VLS 3.5 a) Photograph of the laser equipment used b) Schematic of the lens and its characteristics.

of laser pulses, per linear inch by changing the repetition rate of the pulses in accordance to the speed. In metric units, this parameter ranges from 394 to 39370 pulses per meter and the repetition rate (in Hz) can be calculated by multiplying the repetition rate to the speed of the laser ($m^{-1} \times m.s^{-1}$ =Hz).

The laser setup (figure 3.2) consists in three subsystems: (i) the laser source,(ii) the beam delivery system and (iii) the moving stages. The laser source (i) consists in a CO_2 laser, the beam delivery system (ii) is composed by three mirrors that guide the beam to a focusing lens and the moving stages (iii) position focusing lens relative to the substrate (X and Y axes) and perform the selected pattern to be printed. The vertical positioning (Z axis) is defined by a moving platform on top of which the substrates are placed.

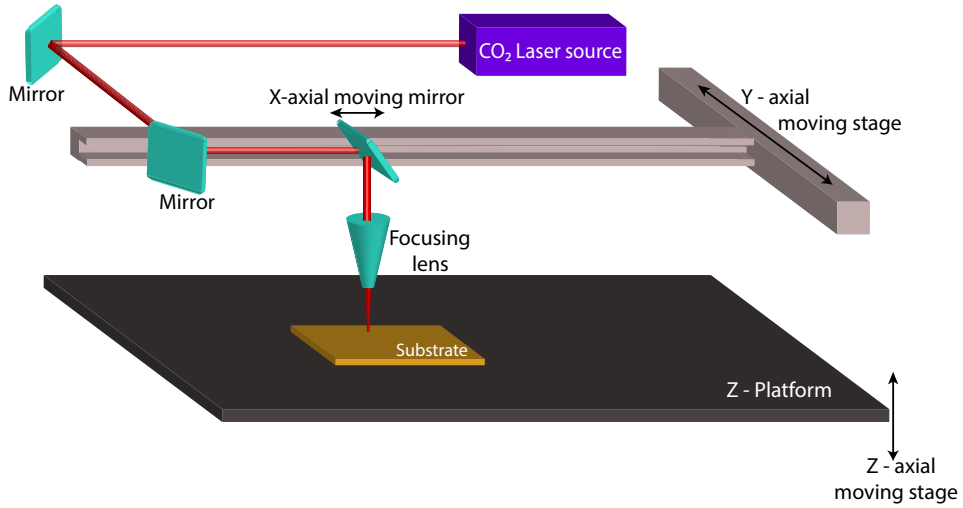

Figure 3.2: Schematic of the laser setup.

3.1.2 Microwave synthesizer

During this work it was used a microwave synthesizer - Discover SP (figure 3.3), a circular single-mode microwave with a magnetron frequency of 2450 MHz. Depending on the solution, the device is capable of heating with a rate from 2 to 6°C/s, with a maximum temperature of 300°C, a pressure of 30 bar and a power of 300 W. At atmospheric pressure, it works in volumes from 0.2 to 75 mL. The microwave interface allows pre-defining synthesis parameters (temperature, pressure, time and power) as well as real-time plotting of these parameters during synthesis.

Figure 3.3: Photograph of the microwave used for the ZnO particles synthesis.

3.1.3 Characterization equipment

Regarding the characterization performed over LIG it was used a SEM - Hitachi TM 3030Plus Tabletop (figure 3.4a), a semiconductor parameter analyzer Keysight Agilent 164442A to measure the IV curves (figure 3.4b) and a Renishaw Qontor Raman microscope with two laser sources (with 532 and 633 nm), with a spectral resolution of 0.3 cm^{-1}, mapping capability with 100 nm of lateral resolution and real time dynamic auto focus, (figure 3.4c).

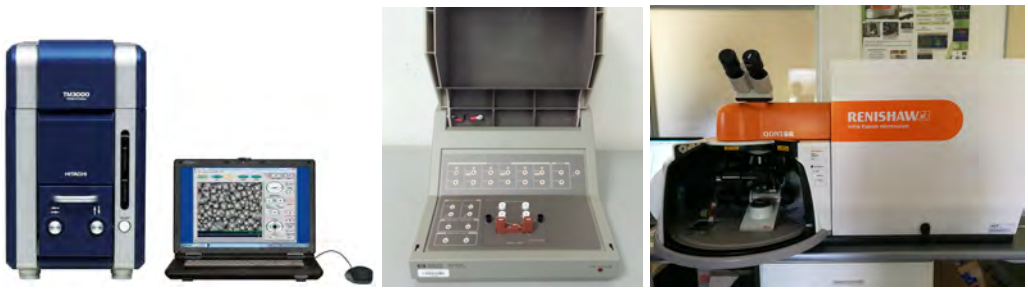

a b c

Figure 3.4: Characterization equipment used in LIG characterization equipment, a) Tabletop SEM, b) Keysight Agilent 164442A, c) Raman microscope.

The study of the synthesized ZnO structures was performed firstly using a commercial X'Pert Pro da PANalytica XRD equipment (figure 3.5a) with a CuKα (K=1.54 $\dot{A}$) source,

an applied voltage of 60 kV and current of 55 mA. For the optical characterization it was used a spectrophotometer UV-Vis-NIR - Perkin Elmer Lambda 950 (figure 3.5b). Lastly a SEM Carl Zeiss AURIGA Crossbeam SEM-FIB and a Oxford INCA xact detector(figure 3.5c) used for the structural and chemical characterization, respectively.

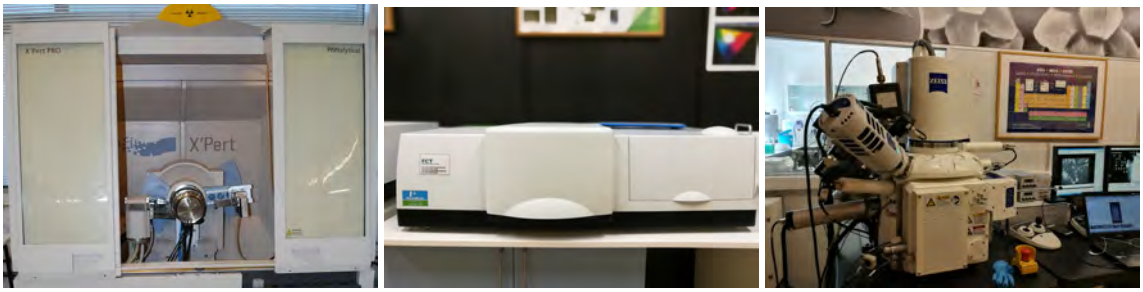

a b c

Figure 3.5: Characterization equipment used for synthesized ZnO particles, a) XRD equipment b) UV-Vis-NIR spectrophotometer, c)Carl Zeiss SEM.

For the UV sensor it was used a contact angle(figure 3.6a) measurement device Dataphysics OCA15plus and a Potentiostat - Gamry Reference 600 for the electrical characterizations (figure3.6b).

a b

Figure 3.6: Characterization equipment used for the UV sensors characterizations, a) Contact angle equipment b) Potentiostat.

3.2 Experimental procedure

3.2.1 LIG fabrication and optimization

The first part of the work consisted in the production and optimization of LIG through a systematic study, in order to find the laser conditions (power, speed and PPI) that result in the best electrical characteristics for both the polymers PI and PEI.

Both polymers were used in sheet format with 75 μm of thickness, PI from Dupont HN and PEI form *McMaster – Carr*, (figure 3.7). All the printed tests were performed by focusing the laser at the surface of the polymer.

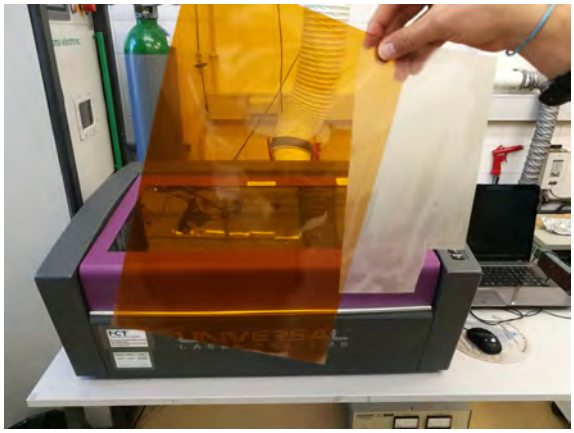

Figure 3.7: Photograph of both polymers PI and PEI.

3.2.1.1 Laser induced graphene formation

The initial and perhaps the most fundamental part of the experimental work was to evaluate which laser conditions lead to the formation of LIG. For the laser-printing, the polymer PI was tape-fixed at the laser working table, figure 3.8b, and lines with 1 cm long and 300 μm wide (figure 3.8a) were laser-printed along several columns with varying parameters. Namely, in each column the speed were kept constant while each line were settled with different powers. The speed was varied between 1.27 m/s and 0.04 m/s, and the laser power between 40 W and 0.1 W.

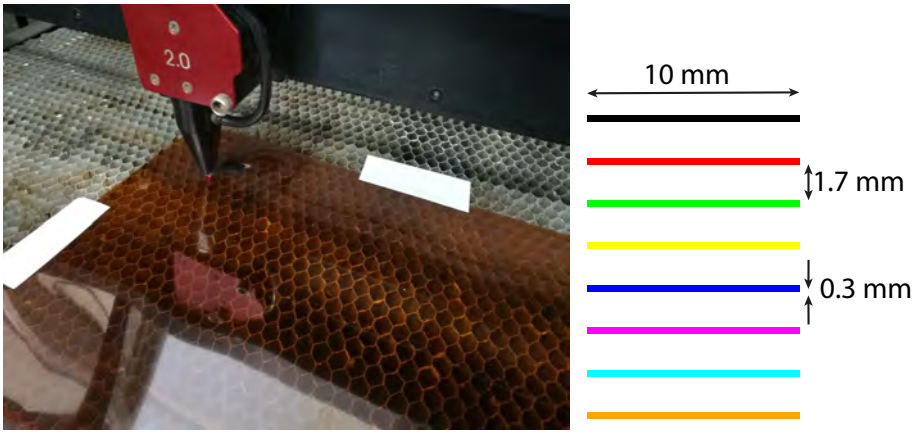

a b

Figure 3.8: LIG first test a) Photograph of the laser table setup, b) Design of the column of lines to be printed in the polymer.

Then, the width of each line was then measured in all lines with an optical microscope

(Olimpus BX51). A preliminary study of the parameters which lead to the formation of LIG was performed by observation of the shape and color of the printed lines.

3.2.1.2 Laser induced graphene electrical characterization

After the preliminary evaluation of the parameters which lead to the formation of LIG, for the sake of statistics and reproducibility, each of those parameters was repeated three times in lines with 0.5 cm long and 300 μm. This allowed performing an evaluation of the electrical properties of the formed LIG as function of the laser parameters. Firstly, IV curves were measured for each line which, by calculating the slope of the curves, allowed calculating the electrical resistances. Then, the thickness of the lines were measured through SEM images of the cross-sections of each line. With the values of electrical resistance, thickness and width (measured in 3.2.1.1), it was possible to determine electrical resistivety.

The following topics report a detailed description of the procedure performed to obtain the values of electrical resistance, thickness and resistance.

- **Electrical resistance measurements**

Silver ink contacts were deposited at the edge of the lines, not only to improve the contact with the probes, but also to ensure that they were always connected at the same distance from each other.

The IV curves were measured using a Keysight Agilent 16442A Test Fixture, by fixing a maximum current of 1 mA (absolute value) while scanning from -0.5 V up to 0.5 V with a step of 0.05 V. The setup used to measure the IV curves is shown in figure 3.9. The electrical resistance was then calculated from the slope of each IV curve with MATLAB.

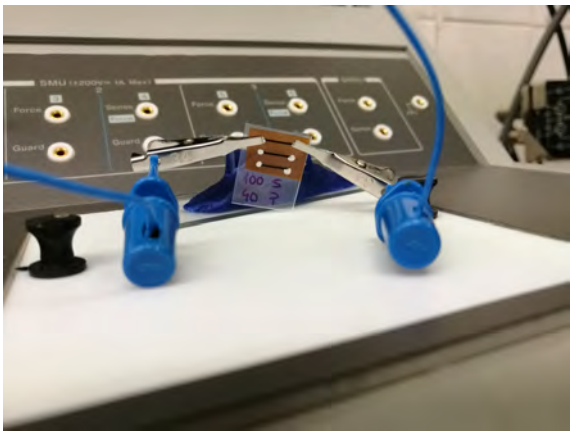

Figure 3.9: Photograph of the setup used at the Keysight Agilent 16442A equipment to obtain the IV curves.

- **Thickness measurements**

The study of the thickness was made through SEM imaging of the cross-sections of the lines. The samples were carefully cut with a scissors and glued to SEM holders, using a double-sized carbon tape (figure 3.10).

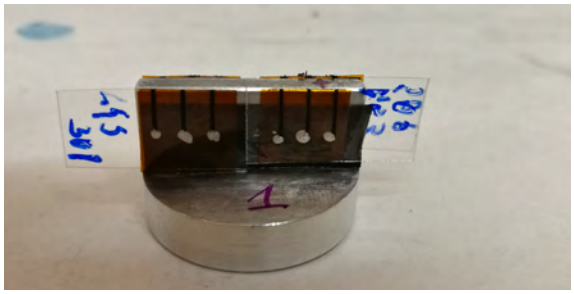

Figure 3.10: Photograph of the samples mounted on the SEM holder.

Then, a coating of 40 nm thick of Au/Pd was deposited by sputtering on the samples and then analyzed using a SEM Hitachi TM 3030Plus Tabletop in order to obtain the cross section images (acceleration voltage of 15 kV and premium Secondary Electrons (SE) detector). The coated layer was added aimed to turn the sample electrically conductive and to avoid charges accumulations.

The thickness was then estimated from SEM images using a Java-based image processing program, ImageJ (National Institute of Health, Bethesda, Maryland, USA).

- **Electrical resistance and sheet resistance**

The width l, the resistance R and the thickness t of the LIG lines, were combined using equation 3.1 to determine the electrical resistivity ρ.

$$\rho = R\frac{t\omega}{l} \tag{3.1}$$

The sheet resistance R_s was then obtained by incorporating equation 3.1 in equation 2.2, resulting in equation 3.2.

$$R_s = R\frac{\omega}{l} \tag{3.2}$$

Both ρ and R_s where calculated for each printed line in order to understand how they vary with the laser power and the laser speed.

3.2.1.3 LIG optimization

A second and more detailed optimization of the laser parameters was performed for laser conditions around those for which the lowest sheet resistance was observed. In addition, a study with the same conditions was performed on PEI. In case the sheet resistance trend showed to be different from PI, a wider and more complete study had to be done.

For each polymer (PI and PEI) the laser parameters were optimized in order to obtain the lowest sheet resistivity.

Having determined the optimal laser power and speed, the effect of the repetition rate PPI was also characterized by keeping the power and speed fixed on the previously optimized values. Then for each line, the sheet resistance was measured as function of the PPI.

3.2.1.4 Additional LIG tests

From the previous studies it was observed how the quality of the laser induced graphene varies for different laser speeds and powers. However there was still a third laser parameter to analyze, the number of pulses per inches.

Thereby it was implemented a study where several lines with different PPI were laser printed, keeping the power and speed always constant on the optimized values found on the previous section. For each line it was measured the sheet resistance and analyzed its behavior as a function of the PPI.

3.2.1.5 LIG Raman spectroscopy

Having optimized all laser conditions, a systematic study of Raman spectroscopy of LIG as a function of the laser power was performed in order to evaluate the quality of the produced graphene stacked structures.

Raman spectra from both PI and PEI were taking from a Reqnishaw Qontor Raman microscope with the green laser with 532 nm of wavelength. Each lasted 1 second for 5 cycles with a power of 50 mW and a grating 600 lines/mm.

3.2.2 ZnO nanoparticles synthesis and characterization

The second main part of the project consisted in the synthesis of ZnO nanoparticles by hydrothermal growth, assisted by microwave irradiation. As a starting point, ZnO nanostructures were synthesized from zinc acetate by microwave-assisted hydrothermal growth, following the procedure described by Pimentel et al. [45].

Two solutions were prepared:(i) solution A - containing zinc acetate dehydrate $Zn(CH_3COO)_2 \cdot 2H_2O$; 98%, Sigma-Aldrich) and sodium hydroxide (NaOH; 98%, Sigma-Aldrich) (ii) solution B - A surfactant dissolution (figure 3.11a).

Solutions A and B were mixed together with 10 mL of Deionized water (DI water) and microwaved for varying exposure time and temperature. The addition of a surfactant solution is frequently used to control the ZnO nanostructures formation aiming to increase the rod length [45].

A systematic study was performed where the influence of concentration, the presence of surfactants and the time and temperature of synthesis were studied.

For the cross-testing of the multiple parameters, a base setting was defined as solution A = 0.5 M of $Zn(CH_3COO)_2 \cdot 2H_2O$ and 8 M of NaOH, and solution B = 10 v/v% Triton X-100, time = 5 minutes and temperature = 120 $^{\circ}C$. Then, three of the parameters were kept constant while the fourth was varied within the following ranges:

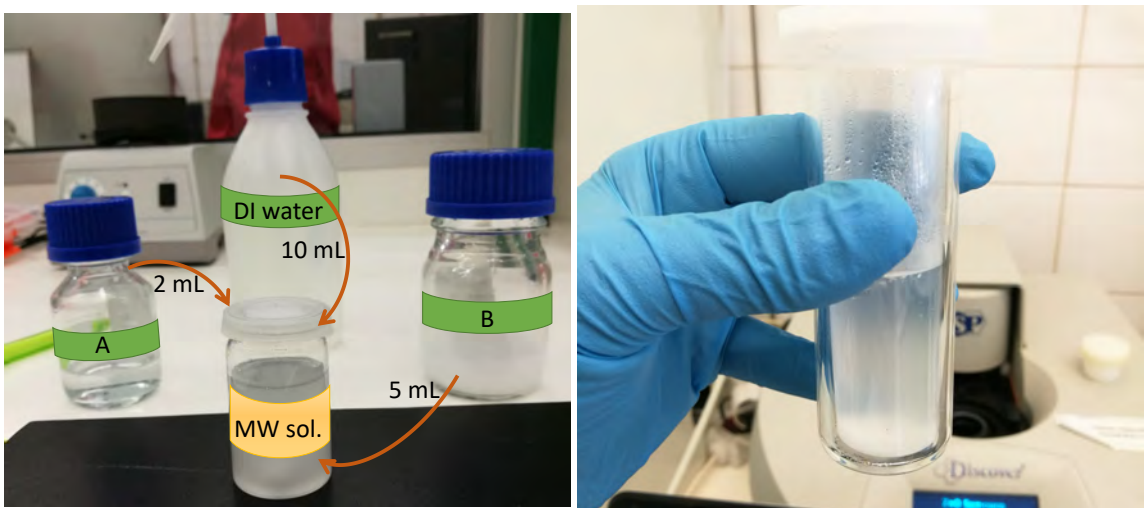

a b

Figure 3.11: ZnO nanoparticles synthesis a) Photograph and schematic of the preparation of the solution to be synthesized. b)Photograph of the solution removed from the microwave after synthesis.

- **Solution A:** 2 mL of solution with concentrations c1(0.25 M of $Zn(CH_3COO)_2 \cdot 2H2O$ and 4 M of $NaOH$), c2 (0.5 M of $Zn(CH_3COO)_2 \cdot 2H2O$ and 8 M of $NaOH$) and c3 (0.75 M of $Zn(CH_3COO)_2 \cdot 2H_2O$ ans 12 M of $NaOH$);
- **Solution B:** 5 mL of a 10 v/v% solution of Triton X-100 (from Sigma-Aldrich), Triton X-45 (from Sigma-Aldrich), or DI water (no surfactant);
- **Microwave exposure time:** 5 minutes, 10 minutes and 15 minutes;
- **Microwave temperature:** 80 $°C$, 100 $°C$, 120 $°C$;

Each of the final solutions for the synthesis were transferred into 35 mL vessels, sealed and placed in the microwave Discover SP. All the synthesis were performed under 100 W of power and a maximum pressure value of 18.62 bar. Once the synthesis were completed, (figure 3.11b), the solutions were washed four times alternating between DI water and isopropanol and centrifuged between each wash during one minute at 4000 rpm. The resulting nanoparticles were then dried in a desiccator at room temperature until completely dry.

3.2.2.1 ZnO nanoparticles characterization

All nanoparticles were carefully analyzed either morphologically and structurally through SEM images and XRD diffractograms and optically by reflectance spectra.

- **SEM characterization**

All ZnO samples were analyzed in the SEM-FIB – Zeiss Auriga CrossBeam Workstation. The preparation for the SEM measurements consisted on the particle dispersion in isopropanol transfer onto silicon carriers, previously cleaned with water, alcohol and a stream of nitrogen. Subsequently a coating of 40 nm Au/Pd was deposited on the samples by sputtering. The images were taken with 15 kV of accelerating voltage.

- **XRD characterization**

XRD was used to determine the crystal structures of the ZnO samples. To do so, the nanoparticles were deposited as a randomly oriented powder onto a sample carrier and subjected to X-rays with a wavelength of 1.54 $\dot{A}$. The measurements were performed using incident angles ranging from 10 to 90 degrees, with a scanning step of 0.33 degrees.

- **Optical characterization**

For the optical characterization, a Perkin Elmer Lambda 950 spectrophotometer was used, where reflectance values were measured for wavelengths between 200 and 800 nm. The nanoparticles were compressed into a powder sample holder to form a compact pellet with 0.5 cm in thickness.

After each measurement the sample holder was cleaned with ethanol and with a compressed air stream to remove any traces from the previous samples. By means of reflectance measurements it is possible to estimate the band gap of ZnO particles [62].

The energy absorbed, or transmitted by a certain material, depends not only on its absorption coefficient α but also on the energy of the incident radiation I_i and the thickness of the absorbing medium d (equation 3.3).

$$I_R = I_i e^{-\alpha d} \tag{3.3}$$

Reflectance is the ratio between I_R and I_i, thereby equation 3.3 it can be re-written as

$$R = e^{-\alpha d} \tag{3.4}$$

From reflectance measurements obtained through the spectrophotometer and the thickness of the pellets, is possible to calculate the absorption coefficient as function of the wavelength. This in turn is related with band gap energy E_g through the Tauc's law, equation 3.5,

$$(\alpha h v)^m = C(h v - E_g) \tag{3.5}$$

where is h is the Planck's constant, C is a proportionality constant, v is the frequency of light and m = 2 (for direct transition mode materials) [63]. From equation 3.5, a Tauc plot can be drawn of $(\alpha h v)^2$ versus $h v$. The point of the extrapolation of the linear part that meets the abscissa corresponds to the value of the band gap energy of the particles.

3.2.3 UV sensor fabrication

The final component of the project consisted on the production of a UV sensor by combining the graphene electrodes made by LIG and the ZnO nanoparticles synthesized by microwave irradiation.

The previously determined ideal laser conditions (power, speed and PPI) (section3.2.1) were used to print interdigital electrodes on both substrates (PI and PEI). The interdigital geometry consists in two interlocking comb-shaped arrays (figure 3.13), a widely used geometry in many applications, including sensors and capacitors [64]. This particular geometry of the electrodes in sensors increases the effective sensing area and consequently the sensitivity of the device to external stimulus, improving the sensor's efficiency.

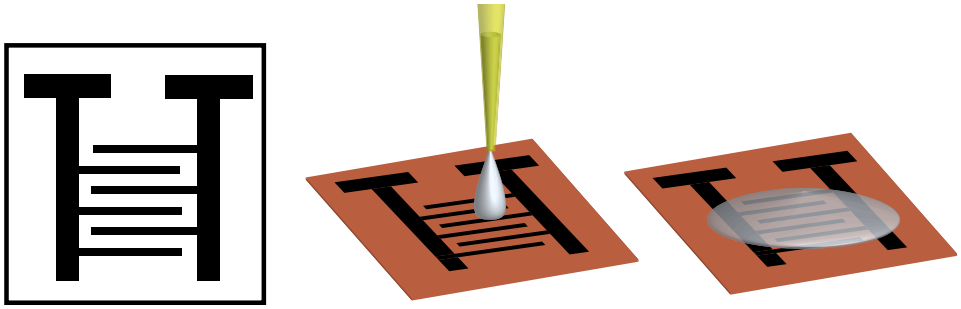

a b

Figure 3.12: Ultraviolet sensor. a) Example of an interdigital electrode geometry, b) Drop-casting of the ZnO dispersion to obtain the final UV sensor.

With the optimized synthesis parameters, a ZnO nanoparticles dispersion with a concentration of 0.127 g/mL was prepared. The interdigital electrodes were subjected to a UV treatment for 15 minutes to render their hydrophilic behavior. Then, 40 μL of this ZnO dispersion was drop-casted onto the interdigital electrodes (figure 3.12b). Once the dispersion became dried, the UV sensors were ready to be tested, figure 3.13a.

To test the sensors, they were subjected to cycles of UV irradiation, while a voltage of 1.0 V was constantly applied at the electrode terminals, (figure 3.13b) and a time-dependent measurement of the photocurrent was performed. The UV irradiation cycles were performed using a UVL-28 EL series UV Lamp with power 8 W and wavelength 365 nm, and the measurements were performed on a potentiostat model 600, from Gamry Instruments, Inc. (Warminster, PA, USA), in a chronoamperometry configuration.

Several UV sensors with different interdigital effective areas were tested with the same conditions for comparison of results. Once the best performance geometry was found, the sensors were also compared with sensors built using commercial components (i) a sensor with carbon-ink (C-200 from Applied Ink Solution) electrodes over PI with custom-produced ZnO nanoparticles dispersion on top (ii) a sensor with LIG electrodes with a 0.127 g/mL dispersion of commercial ZnO nanopowder, with a particle size <100 nm from Sigma-Aldrich Chemistry.

It was also tested the flexibility of the UV sensors by placing them on round molds with radius of curvature of 45, 25 and 15 cm (figure 3.13c).

Furthermore, to test the stability of the sensor long-term behavior, the PI sensor was tested in the UV exposure configuration for a ten-hours assay.

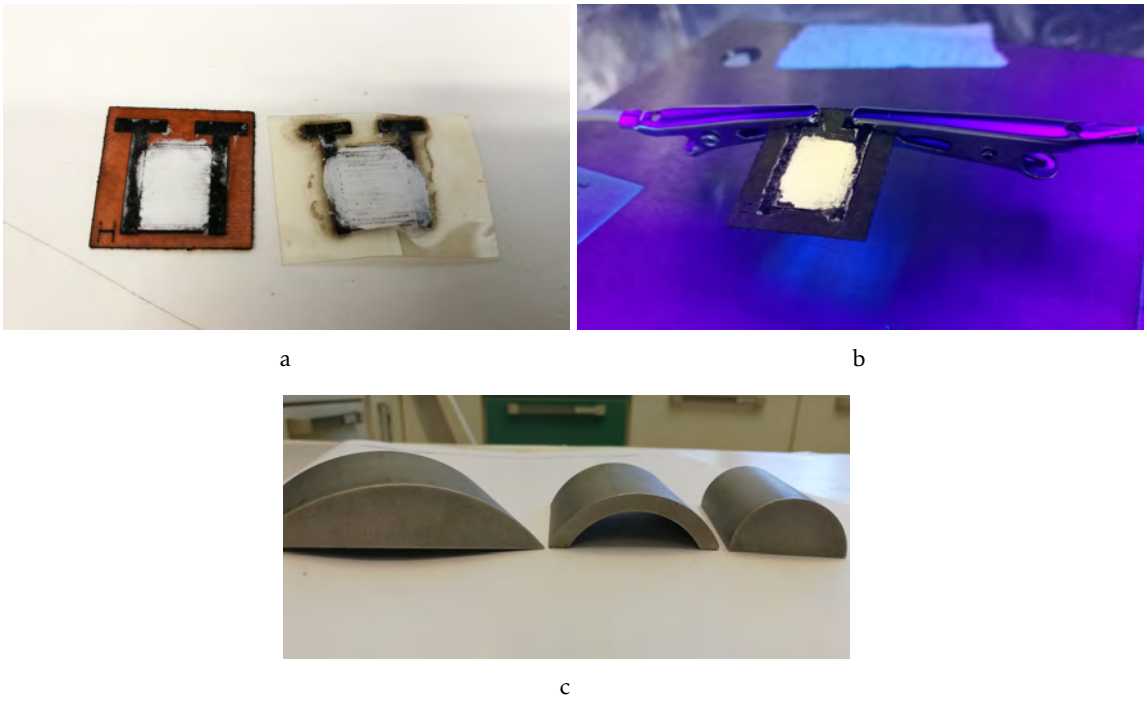

a b

c

Figure 3.13: Final ultraviolet sensors. a) Photograph of the final sensors made in the two substrates, PI and PEI b) Photograph of an UV sensor being irradiated with an ultraviolet light, c) Photograph of the round molds used to test the flexibility of the UV sensors.

3.2.4 Production of electrodes in paper by laser direct writing

Additional tests were carried out in testing electrodes in paper using the laser direct writing technique. Paper has been the target of extensive investigation regarding its integration electronics and optoelectronics. The strong interest on this material is mainly due to its easy access, flexibility and mainly its production cost, allowing low-cost applications [65].

The possibility of combining the production of electrodes through laser direct writing technique and paper open doors for the design of electronic devices without the need of controlled atmosphere and high temperature, with the advantage of using flexible and easy access materials, making the devices extremely inexpensive to implement.

Under the light of such motivation, it was attempted to produce laser induced silver and copper electrodes on paper subtracts. In the next two sections the procedure for the production of silver and copper electrodes is presented.

3.2.4.1 Laser induced silver electrodes

For the silver electrodes, it was prepared a 1 M solution of silver nitrate ($AgNO_3$ from Sigma-Aldrich). A sheet of Whatman paper number 1 from GE Healthcare UK was soaked in the solution for 10 minutes, figure 3.14, and it was let to dry at room conditions, [21].

The dry paper was transported to the laser desk and several lines with 5 mm long and 0.3 mm wide were printed with 3.5 W of CO_2 laser power and speeds of 0.76, 0.64, 0.50 and 0.38 m/s.

Figure 3.14: Silver electrodes preparation. Photograph of the 1 M $AgNO_3$ solution and soaked paper.

The laser-induced silver electrodes were electrically analyzed in the Keysight Agilent, to obtain the IV curves and respective electrical resistance. The applied voltage made to vary from -1 V to 1 V, with a defined maximum absolute current value of 1 mA. The samples were also observed in the SEM-FIB – Zeiss Auriga CrossBeam Workstation where the top and cross-section views were analyzed.

3.2.4.2 Laser induced copper electrodes

For the copper electrodes a solution inspired in the paper [20] was prepared, with 60 wt % of copper oxide (CuO from Sigma-Aldrich), 13 wt % of polyvinylpyrrolidone (PVP M_w 10 000,from Sigma-Aldrich) and 27 wt % of ethylene glycol from Carlo Erba.

The resulting solution was brushed onto *whatman* paper number 1 and left to dry at room conditions. Once dried, the paper was placed on the laser desk and a line with 5 mm long and 0.3 mm wide was laser printed with 3.5 W of power and 0.38 m/s of scanning rate.

Chapter 4

Results and Discussion

In this chapter the main results obtained throughout this master thesis are presented an discussed, in correlation with theoretical concepts and results obtained previously by other research groups.

The chapter is divided into four sections: Section 4.1 presents the results of the production and optimization of laser-induced graphene for enhancement of its electrical properties both in PI and PEI; Section 4.2 shows the results of ZnO nanostructures synthesis and characterization using multiple optical, crystallography and microscopy techniques; Section 4.3 describes the characterization and optimization of UV sensors built using the optimized components studied in Sections 4.1 and 4.2; Finally in section 4.4 it is presented the results obtained for the production of laser induced silver and copper electrodes on paper substrates.

4.1 Optimization of LIG-produced electrodes in different substrates

4.1.1 Laser induced graphene in PI

The study of LIG in PI started with a generalized procedure where the laser powers and speeds in which LIG occurred were identified. It followed a more detailed study of the electrical and structural properties and lastly LIG was optimized to enhance its electrical properties by varying the laser parameters.

4.1.1.1 Identification of laser parameters for LIG

As it has been mentioned in the section 3.2.1.1, the first step of the LIG optimization consisted on a systematic study probing for the optimal laser conditions for the formation of

LIG in a PI polymer surface. The study was performed by testing multiple combinations of laser power and speeds, laser-printed onto a single PI sheet in a matrix-like arrangement (see figure 4.1). In this arrangement, the columns correspond to scanning speeds and the rows to laser power.

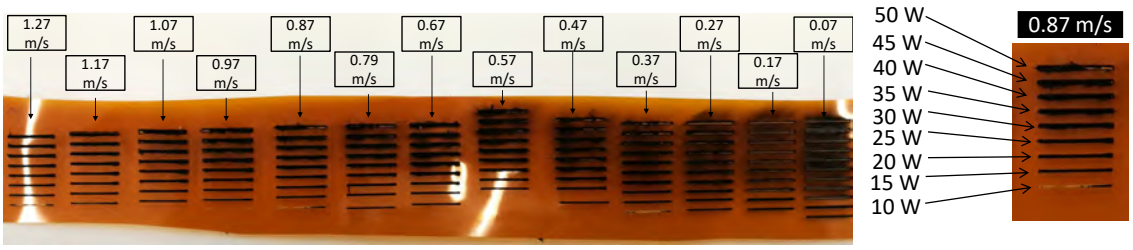

a b

Figure 4.1: Photographs of the first LIG test in PI. a) Photograph of some columns each with different speeds. b) Photograph of a column with different laser power in each line.

This study allowed, by the color change of the polymer after the laser irradiation, to identify three distinct laser power and speed regions which cause different aftereffects in the polymer. On the one hand, for high scanning speeds but low laser powers, the amount of energy transmitted to the polymer is not large enough to break the chemical bonds necessary for LIG to occur, hence there is no carbonaceous material formation. An example of such case can be observed in the last laser-printed line of figure 4.1b. On the other hand, for high laser powers and low scanning speeds, the energy that is impinged on the polymer becomes high enough to break all chemical bonds without undergoing the recombination process that is required for the formation of LIG. Instead, the PI is punctured and becomes permanently damaged, with occasional formation of LIG around the edges of the perforation, due to an uncontrolled thermal energy dispersion gradient. An example of such can be observed in the top line of figure 4.1b. The results therefore demonstrate that the formation of LIG can only be obtained with a combination of laser power and scanning speed, such that the amount of energy provided to the polymer is high enough to break the C-O, C=O and N-C bonds (in which case LDWM), but not so high that it drills through the polymer.

The results of the aftereffects in PI are summarized as function of laser power and scanning speed in figure 4.2a. In this plot, grey regions represent non-formation of LIG due to insufficient energy, the green regions represent effective formation of LIG and the red regions represent polymer-drilling by excessive energy.

Additionally, the laser-printed lines were characterized using an optical microscope, which revealed that also the width of the printed lines varied with power and speed (see figure 4.2b). In fact, all printed lines, were designed with a fixed nominal width of 300 μm, which means that the lateral thermal energy dispersion on the surface of the polymer, as function of the laser conditions must also be taken into consideration in the design of

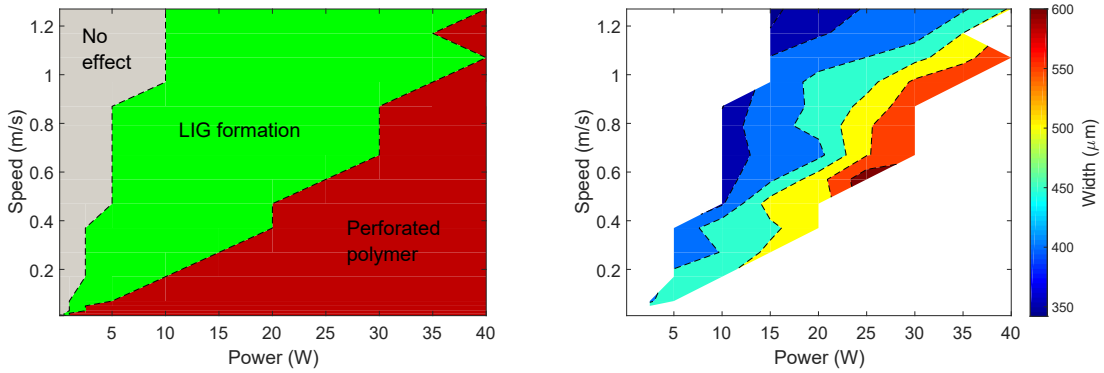

a b

Figure 4.2: Results of the first LIG test in PI. a) Plot of the three different laser power and speed regions that causes different aftereffect in the polymer. b) Results of the width measurements in μm as a function of the laser power and the scanning speed.

LIG electrodes for instance in sensor devices. In this sense, lower laser-powers and higher speeds correlate with lower thermal energy dispersion and therefore thinner lines, and higher laser power correlates with wider lines (figure 4.2b).

4.1.1.2 LIG electrical and structural characterization

After optimization of the laser parameters for the formation of LIG, a study of the electrical properties of the obtained structures was performed, by the measurement of IV curves in accordance to the method described in section 3.2.1.2.

Figure 4.3a shows an example of one of the measured IV curves, where a linear regression has been used to determine the electrical resistance, by calculating the inverse of the slope of the linear regression. This particular plot shows the results from laser-printed line under 2.5 W and 0.01 m/s of laser power and speed, respectively, for which a resistance of 357 Ω has been calculated.

This analysis has been repeated for all printed lines, with laser parameters lying within the green region of figure 4.2a, and the results were grouped into a filled-contour plot of electrical resistance as function of laser power and scanning speed (figure 4.3b). The results showed that the electrical resistance of the printed lines are not independent from the laser conditions. Indeed, a variation in the resistance from 3500 down to 200 Ω has been observed, where the minimum values occur for lower speeds and powers.

Surface characterization of the optimized LIG structures has been performed using SEM In order to further analyze the cross section profile of LIG and measure its thickness, the samples with the lowest electrical resistances were analyzed in the SEM following the procedure described in 3.2.1.2. Table 4.1 shows part of the obtained SEM images of the LIG cross-sections images and figure 4.4 resumes the thickness measurements for different laser parameters.

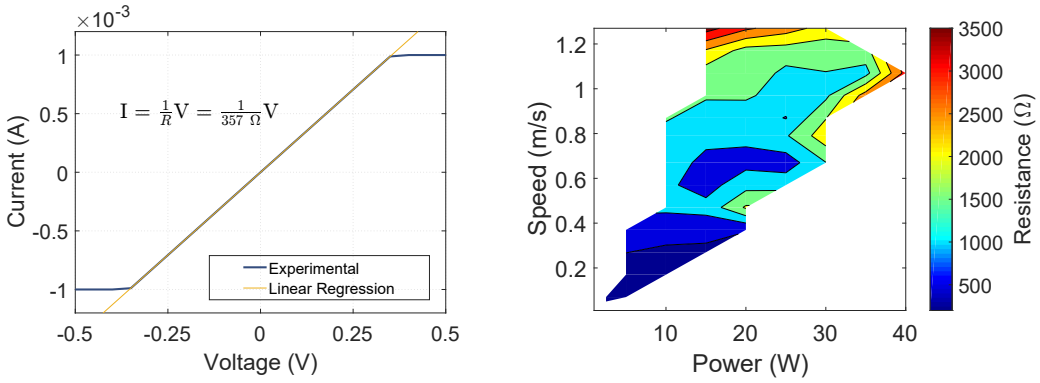

a b

Figure 4.3: Results of the resistance measurements. a) IV curve and respective fit of the laser printed line made with 2.5 W of laser power and 0.01 m/s of speed, for which a resistance of 357 Ω has been calculated b) Contour plot of the electrical resistance (in Ω) in function of the laser power and speed.

Table 4.1: Selection of some SEM images of the LIG cross sections for different laser powers and speeds.

	0.17 m/s	0.37 m/s	0.57 m/s
7.5 W		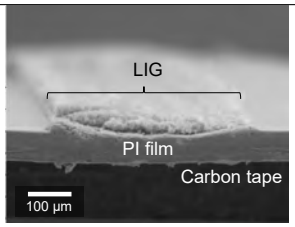	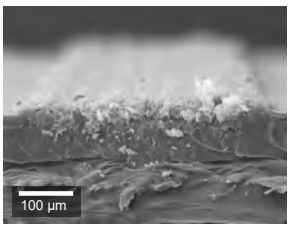
10 W		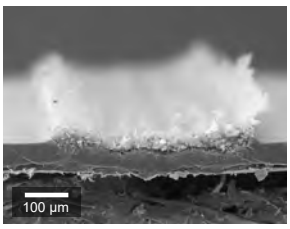	
20 W		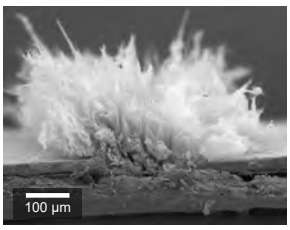	

The results show a strong dependence of the LIG profile on the laser power, where higher powers yield thicker and rougher surfaces (in some cases looking almost *hairy*). On the other hand, the scanning speed does not exhibit significant effects on the profile and thickness. A possible reason for this is that the speed only changes the time of irradiation in each spot, but has no impact on the amount of energy per unit of time being delivered

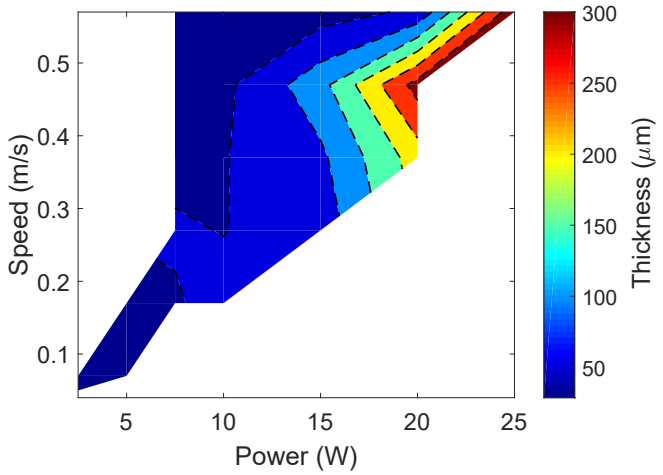

Figure 4.4: Results of the thickness measurements. Contour plot of the thickness in function of the laser power and scanning speed.

to the system. Therefore, it is indeed the power that seems to have a stronger effect on the reaction depth and consequently, the thickness.

Using the measured width, resistance and thickness, the electrical resistivity was calculated (through equation 3.1) in order to study how it is influenced by the laser parameters. The results are shown at the log plot of figure 4.5, where the electrical resistivity is presented as a function of the laser power for different scanning speeds.

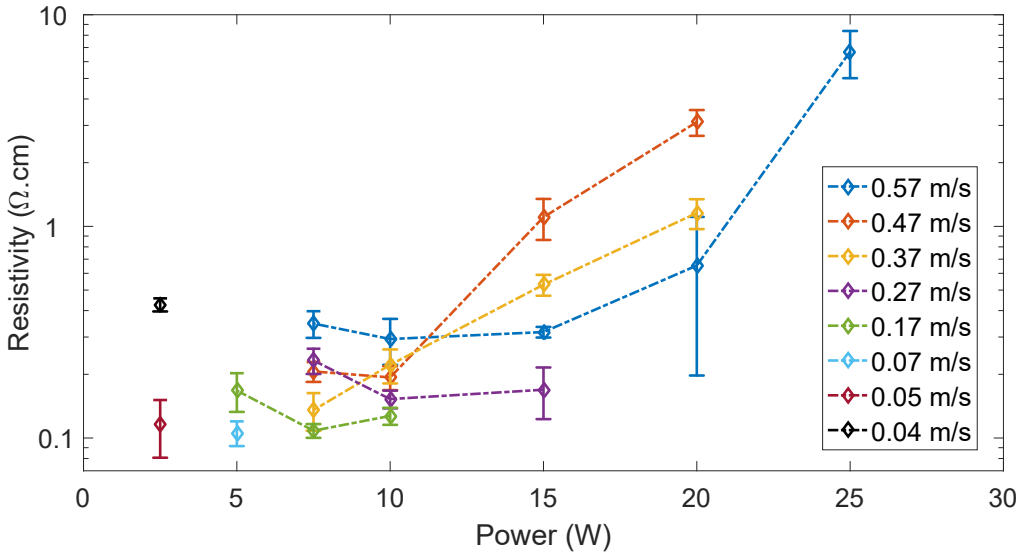

Figure 4.5: Electrical resistivity results. Log-lin plot of the resistivity behavior as a function of power for different speeds.

The results revealed that lower the powers yield lower electrical resistivities. This effect may be correlated to the higher density and more homogeneous films observed

in the SEM images also for lower powers (table 4.1). In that sense, denser and more homogeneous films enhance the electron mobility, thus lowering the resistivity.

To be able to compare the electrical properties of LIG with literature, the sheet resistance R_S was determined, using equation 3.2, for different values of power and velocity. The results are shown on the filled-contour plot of figure 4.6. Again, sheet resistivity was observed for the lower laser powers and scanning speed. These results are compared with literature in section 4.1.1.3.

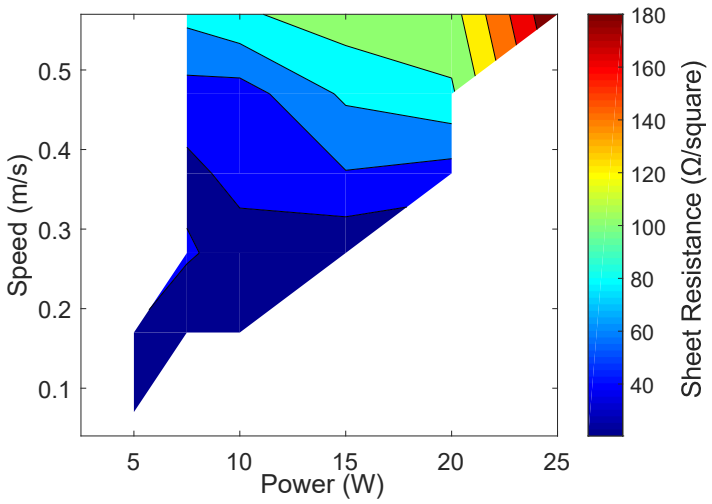

Figure 4.6: Contour plot of the sheet resistance in Ω/*square* for different laser power and scanning speeds.

4.1.1.3 LIG optimization

In order to find the laser conditions in which it is obtained the lowest sheet resistance, experiment described in 3.2.1.2 was repeated with higher resolution on the lower speeds and powers.

The results are shown in the plot of figure 4.7a. The minimum sheet resistance obtained was 19.75 Ω/square for a laser power of 7 W and a scanning speed of 0.1 m/s, which is in line with the 15 Ω/square presented by Lin and al [17], in figure 4.7b. Furthermore, the data from figure 4.7a shows that a minimum in the sheet resistance was reached for some speeds. Lin et al also observed two distinct slopes of Rs versus laser power and justified it to be an effect of the influence of the thermal power on the graphitization. The higher the power, the higher the graphitization level, which leads to an increase of the quality of the film and decrease of the sheet resistance. However, from a certain laser power the oxidation starts to play an increasingly deleterious role in the quality of the films, which rise the sheet resistance. This effect has been observed for powers between 8.5 and 10 watts.

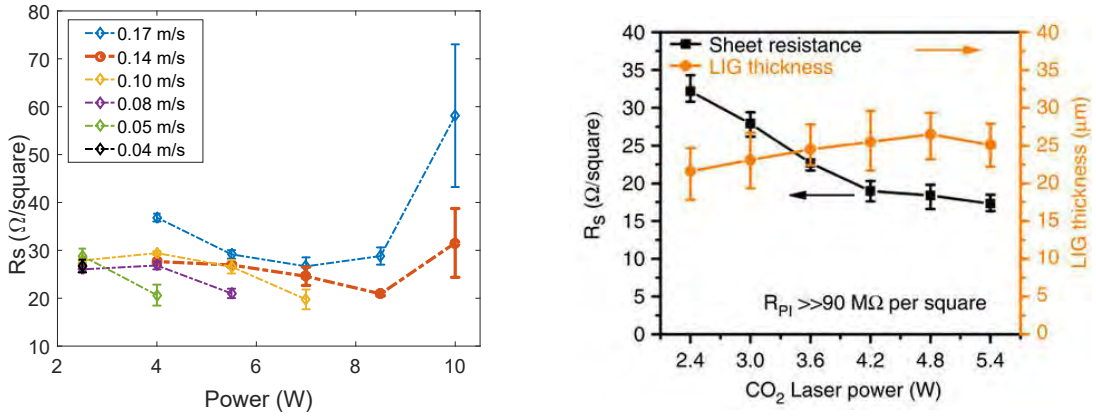

a b

Figure 4.7: LIG optimization in PI. a) Sheet resistance obtained in function of laser power for different scanning speed. b) Sheet resistance obtained by Lin et al[17] for a scanning speed of 0.9 m/s.

It has also been observed that the minimum sheet resistance obtained for the different conditions rounded 20 Ω/square. However, the formation of LIG for speeds between 0.04 and 0.10 m/s is limited to relatively low powers and slow fabrication process. Hence, sheet resistance-wise, a speed of 0.14 m/s and laser power 8.5 W, seem to be promising conditions for the production lines with low sheet resistance in a fast and reproducible manner.

For the determined optimal conditions, several lines were printed with varying PPI. The sheet resistance was determined for every printed line and the results were plotted in figure 4.8.

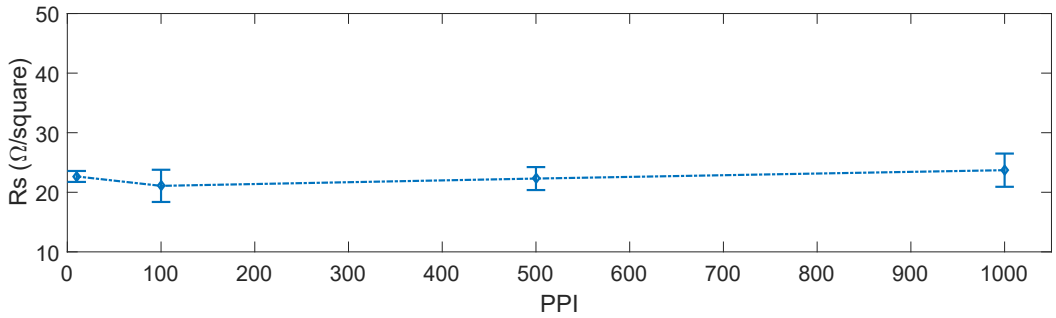

Figure 4.8: Variation of sheet resistance as a function of the pulses per inches for a laser power of 8.5 W and a scanning speed of 0.14 m/s.

The results show no significant influence of the PPI in the LIG sheet resistance, with the exception of 100 to 10 PPI where it is visible a slightly increase in sheet resistance. This effect can be justified by considering the lateral overlap of the thermal spread at the polymer surface upon laser excitation. Assuming the radius of the thermal spreading to

be much larger then the 127 μm laser spot size, relatively small variations in the pulse spacing (from 100 to 1000 PPI) lead to small effect on the lateral overlap of the thermal spread and therefore produce nearly no change in homogeneity of the irradiated surface. For relatively long pulse-spacing however (from 10 to 100 PPI), the overlap becomes much smaller and the heterogeneity on the irradiated surface starts to affect the LIG sheet resistance (figure 4.9).

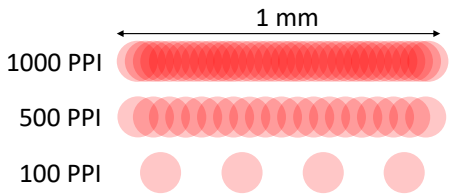

Figure 4.9: Representation of the laser spot size spacing for different pulses per inches: 0.025, 0.051 and 0.254 mm for 1000, 500 and 100 PPI, respectively.

Given the lack of effect of the PPI, all LIG tests following this experiment were performed using the maximum allowed value of pulses per inches, 1000 PPI.

In order to analyze the quality of LIG, a systematic study of Raman spectroscopy was performed, over the samples obtained with 0.14 m/s of a laser of speed and powers varying from 4 W to 10 W (figure 4.10).

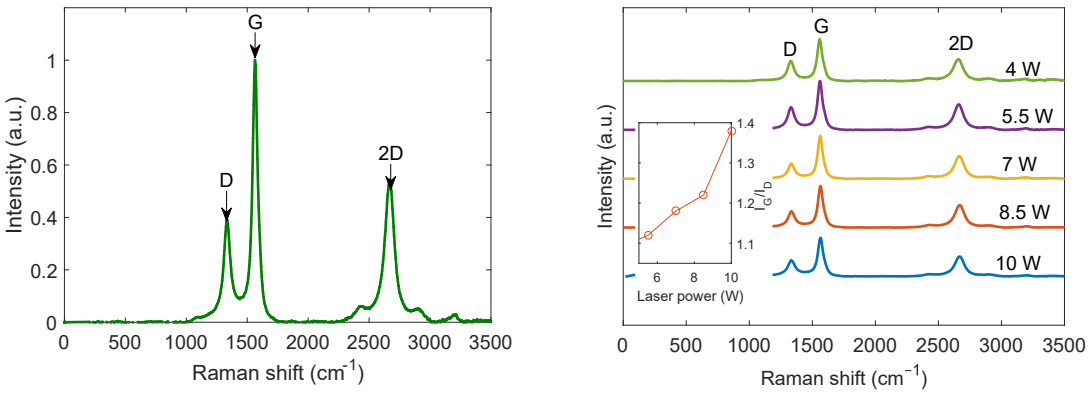

a b

Figure 4.10: Raman spectra of LIG in PI(obtained with a green laser with 532 nm) a) For the optimized laser conditions, 8.5 W and a 0.14 m/s of laser power and speed, respectively b) In function of the laser power and the respective ratios of peaks intensities G and D.

In all spectra it is observed the three Raman peaks features of graphene and graphitic materials, the D, G and 2D at 1336, 1563 and 2670 cm^{-1} respectively (figure 4.10a). The D peak is induced by defects, disordered in hexagonal graphitic layers and amorphous carbon species, these defects are present at the edges of graphene sheets but appear in great quantities in graphene stacked structures. The intensity ratio of D and G bands

Table 4.2: Intensity ratios of the Raman peaks as a function of the laser power for a speed of 0.14 m/s.

Laser power (W)	**4.0**	**5.5**	**7.0**	**8.5**	**10.0**
I_{2D}/I_G	0.93	0.90	0.89	0.86	0.76
I_G/I_D	1.09	1.12	1.18	1.22	1.38

(I_D/I_G) is then used to determine the quality of graphitization or defective disorders on the crystalline graphite. The G peak is caused by the first-order scattering of the in-plane optical phonon reflecting the lattice symmetry of graphene and order degree of carbon atoms and the 2D peak result of a second-order process involving two phonons with opposite momentum [66, 67]. The intensity ratio of I_{2D}/I_G is commonly used as an indication of the nature of the graphene layers, particularly, $I_{2D}/I_G > 2$ is a typical feature of monolayer graphene. For the LIG formed with 8.5 W and 0.14 m/s of laser power ans speed respectively (parameters which revealed lower sheet-resistance, spectrum plotted in figures 4.10a), a I_{2D}/I_G ratio of 0.86, which suggests graphene stacked structures. On the other hand, the presence of the D peak and the ratio I_G/I_D of 1.22 suggests a moderate density of lattice defects, activating the D band, usually nonexistent in for monolayer graphene.

The intensity ratio of I_{2D}/I_G observed in the systematic study of Raman spectra as a function of the laser power (figure 4.10b and table 4.2) increases with the decrease of the laser power, suggesting a stronger monolayer character for lower laser powers. Additionally, the I_G/I_D ratio tend to increase with the laser power, implying a decrease of the number of defects.

Overall, the sheet resistance and the Raman spectrocopy results indicate that a power of 4 W, speed of 0.05 m/s and PPI of 100 would be the optimal laser conditions for the formation of LIG. However, a speed of 0.14 m/s, 8.5 W and PPI of 1000 were used in order to increase the fabrication speed, while still guaranteeing the formation of good-quality LIG.

4.1.2 LIG in PEI

After optimizing the laser parameters for PI, the next step was to determine the ideal parameters for PEI.

The used PEI sheets have two different sides, a rough and a smooth one. The first test was to evaluate which of the surfaces would best suit the formation of LIG (figure 4.11).

The smooth side showed a more uniform behavior and lower values of sheet resistance. This effect can be justified by taking into account the dispersion of light at the material's surfaces. Upon irradiation of the rough surface, light scatters in all directions due to the microscopic irregularities of the interface, leading to a energy absorption process that is less efficient and less reproducible then for smooth surfaces. Therefore, the smooth side was chosen to perform all following studies.

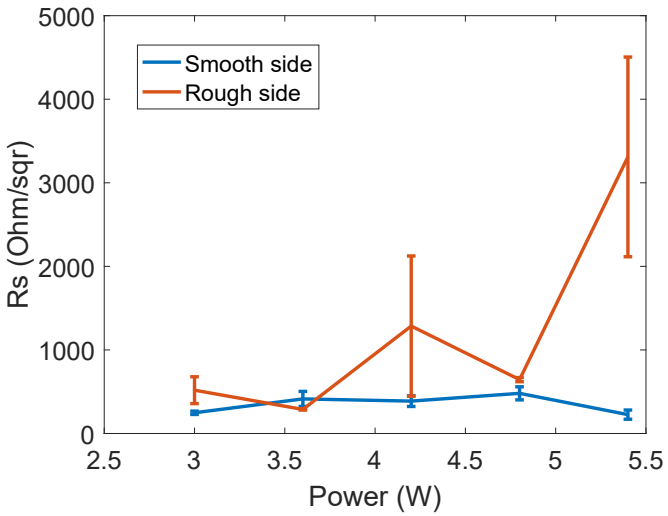

Figure 4.11: Sheet resistance calculated both for the rough and smooth size of PEI in function of the laser power for a scanning speed of 0.17 m/s.

4.1.2.1 LIG optimization

From the previous study with PI, it was concluded that the LIG with the smallest sheet resistance was obtained for lower powers and speeds. Therefore the for experiments performed with PEI were performed using as a start-point the laser parameters region already known to be the ideal region for the best LIG. The sheet resistance calculated for PEI in function of the laser power for different scanning speed are shown in figure 4.12.

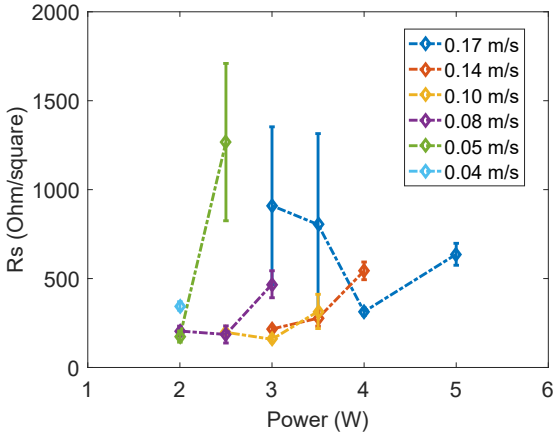

Figure 4.12: Sheet resistance for PEI in function of the laser power for different a scanning speed.

The minimum sheet resistance obtained was 158.7 $\Omega/square$ for a laser power of 3 W and a scanning speed of 0.1 m/s. Again, as it happened with PI it is observed minimums in the sheet resistance due to the consequences of the thermal power and oxidation on the graphitization already explained in 4.1.1.3.

For an estimate of the thickness of the LIG produced in PEI, three samples were imaged by SEM, by measuring cross-section images under the same conditions as those of PI. Three of such images are shown in table 4.3, where an increase in thickness and surface roughness was observed for higher laser powers.

Table 4.3: Selection of some SEM images of the LIG in PEI cross sections for a scanning speed of 0.10 m/s for the laser powers of 2.5, 3 and 3.5 W.

2.5 W	3 W	3.5 W
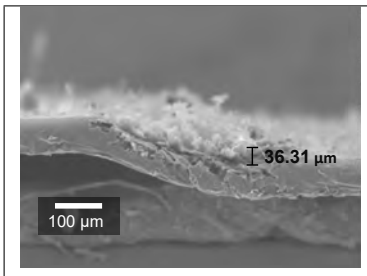	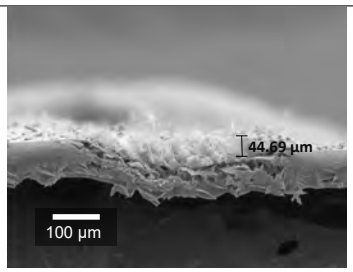	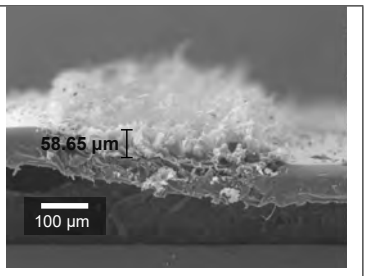

Additionally, the quality of the LIG in PEI was evaluated using Raman spectroscopy (figure 4.13). The three Raman peaks characteristic of graphene D, G and 2D are again visible at 1341, 1584 and 2665 cm^{-1}. The G peak, generated by the defects in the lattice, is found in the spectrum with high intensity ($I_G/I_D = 1.23$), which indicates a big density of defects and a disordered lattice structure indicating the presence of amorphous carbon. In addition, a ratio of 0.26 for I_{2D}/I_G was observed, which suggests a big number of graphene layers.

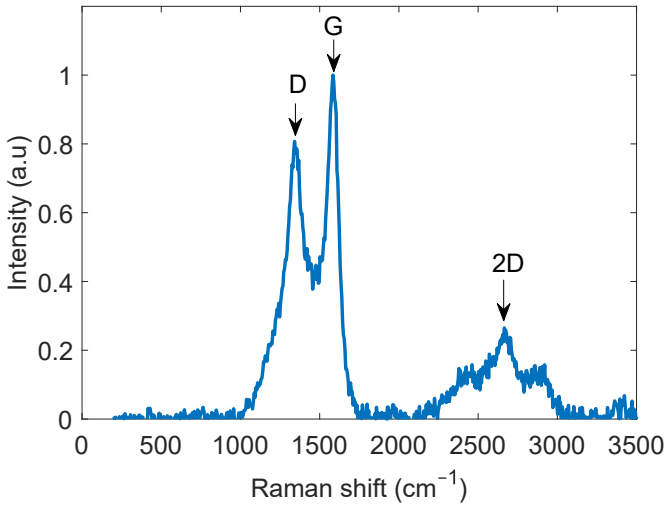

Figure 4.13: Raman spectra of LIG in PI for a laser power of 3 W and 10 m/s of scanning speed.

4.1.3 Comparison and discussion of results

From the initial study with PI it was verified that there is a well defined region of laser parameters for which there is formation of LIG. For other parameters outside this region, the laser can either drill the polymer or produce no changes.

The laser parameters seem to have a big influence on the LIG characteristics. The laser power influences the width, thickness and resistivity, which became smaller for lower powers. Also, the LIG profile changes with the power, the smaller the power the less *hairy* and more compact the sample is.

However it is visible some differences in the LIG formed on both PI and PEI polymers. For example, the uniformity of the LIG varies in the two polymers. When the polymers were observed under the microscope PI showed much more uniform LIG than PEI, which instead showed a higher porosity (figure 4.14). Nevertheless, PEI substrate allowed a better lateral resolution, of 152 μm, when comparing with the 186 μm from PI.

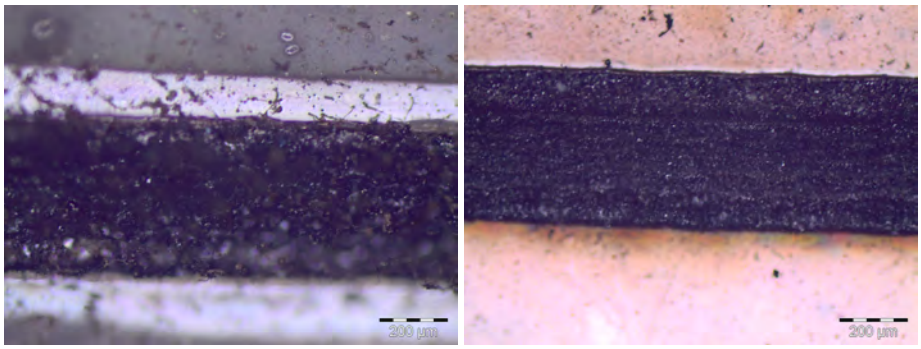

a b

Figure 4.14: LIG microscope image obtained for 0.07 m/s and 2.5 W laser speed and power respectively for a)PEI and b)PI.

The lowest sheet resistance was observed for lower laser powers and scanning speed. Figure 4.18a shows the lowest sheet resistances obtained both for PEI and PI in function of the laser power, for scanning speed of 0.10 and 0.14 m/s respectively.

The minimum sheet resistance obtained for both polymers have a difference one order of magnitude between them. For PI laser conditions chosen to further implement in the sensors was 8.5 W and 0.14 m/s where it is reached a sheet resistance of 20.91 $\Omega/square$. For PEI, the sheet resistance reached a minimum value of 158.7 $\Omega/square$ for 3 W of laser power. On the one hand, it is required a higher power to obtain the best LIG for PI then for PEI but on the other PI presents a much lower sheet resistance.

From Raman spectra both polymers shown evidence of graphitic materials where the laser passed by through the presence of the three peaks D, G and 2D.

The Raman spectra of both polymers showed evidence of graphitic materials, where the laser passed by through the presence of the three peaks D, G and 2D. However, the intensity of the peaks in PEI were much lower when compared with PI, which suggests

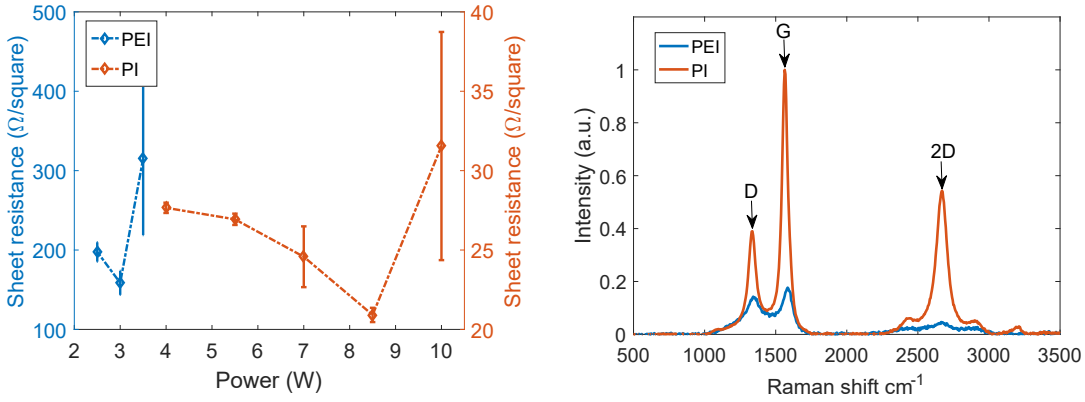

a b

Figure 4.15: Comparasion of LIG from both polymers PEI and PI. a) Lowest sheet resistances for PEI and PI for 0.10 and 0.14 m/s respectively. b) Normalized Raman spectra for PI and PEI.

a lower graphene quality. This conclusion is reinforced by the I_D/I_G ratios of 0.39 for PI and 0.81 PEI. These values indicate a moderate density of lattice defects on the LIG formed in PI and a disordered lattice structure. Such features suggest the presence of amorphous carbon for the LIG formed in PEI. Additionally, a blue shift of about 21 cm^{-1} on the G band was observed from the PI to the PEI spectra, which is possibly attributed to the reduction in size of the in-plane sp^2 domains maybe due to a strong oxidation of graphite [68]. Furthermore, comparing the I_{2D}/I_G ratio of both polymers (0.54 and 0.26 for PI and PEI respectively) propose a higher number of graphitic layers.

Overall, both polymers were shown to be capable of forming LIG, however, PI presents a LIG with lower sheet resistance and the Raman spectra reports a better quality of the LIG produced in this polymer. As proof of concept of the electrodes produced on both materials, a simple circuit with an LED was implemented. This assay expressed the advantage of freedom of design provided by the laser direct writing and conductivity of the produced films (figures 4.16a and 4.16b).

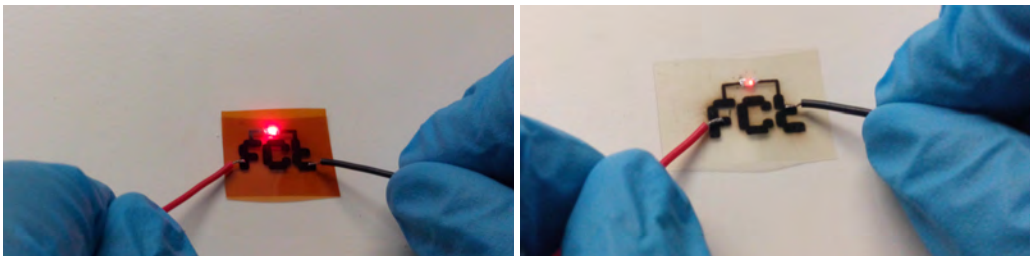

a b

Figure 4.16: Proof of concept for the optimized LIG for PI and PEI. Photograph of a ON state LED connected to an optimized graphene electrode in a) PI ans in b)PEI.

4.2 Characterization of synthesized ZnO particles

Regarding the fabrication of ZnO nanoparticles, a study of the synthesis parameters was performed in order to enhance the surface/volume ratio. The experimental parameters were: the concentration of the zinc acetate and sodium hydroxide solution (solution A described in section 3.2.2, the presence of a surfactant, solution B, and the synthesis time and temperature, defined on the microwave device).

Table 4.4 expresses a simple nomenclature used throughout this report for a clearer referencing of the solutions used.

Table 4.4: Nomenclature of the synthesized ZnO nanoparticles. T stands for Trinton. $ZnC_4H_6O_4$ is the short formula of $Zn(O_2CCH_3)_2 \cdot (H_2O)_2$ for zinc acetate. NaOH stands for sodium hydroxide

Variable	Name	Conditions	
Solution A	c1	0.25 M $ZnC_4H_6O_4$ 4 M NaOH	1/10 v/v Tr X-100 5 minutes 120 ºC
	c2	0.5 M $ZnC_4H_6O_4$ 8 M NaOH	
	c3	0.75 M $ZnC_4H_6O_4$ 12 M NaOH	
Solution B	x100	1/10 v/v Tr X-100	0.5 M $ZnC_4H_6O_4$, 4 M NaOH 5 minutes 120 ºC
	x45	1/10 v/v Tr X-145	
	NoSurf	Deionized water	
Synthesis time	5 min	5 minutes	0.5 M $ZnC_4H_6O_4$, 4 M NaOH 1/10 v/v Tr X-100 120 ºC
	10 min	10 minutes	
	15 min	15 minutes	
Synthesis temperature	T80	80 ºC	0.5 M $ZnC_4H_6O_4$, 4 M NaOH 1/10 v/v Tr X-100 15 minutes
	T100	100 ºC	
	T120	120 ºC	

Each parameter was changed individually leaving the other parameters of the solution and synthesis intact.

An important detail of the microwave-assisted synthesis regards to the heating time of microwave device (figure 4.17). At the initial moment the temperature increases from room temperature until the temperature setpoint - heating ramp. The synthesis duration is defined from the moment at which the temperature setpoint is reached to the moment of beginning of temperature cool-down. The cool-down is aided by a jet of nitrogen and at temperature of 50 $^{\circ}C$ the microwave door opens and the sample can be removed.

Physically however it is difficult to determine the exact momento of beginning of reaction, meaning that part of the reaction also occurs during the heating and cooling ramps. Yet another issue is that the time of each heating ramp can vary from sample to sample, depending on the starting temperature, the number of molecules in solution with polarity, and time-dependent pressure profile, which varied considerably from sample to sample and is difficult to control.

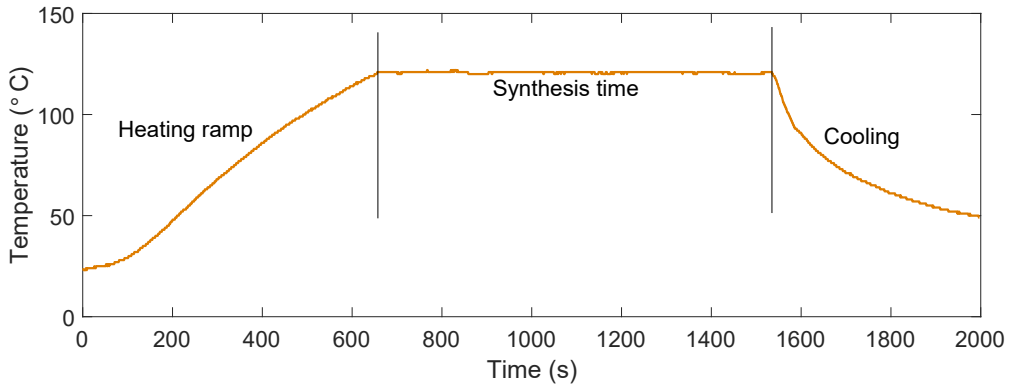

Figure 4.17: Plot of the temperature in function of time during one of the ZnO nanoparticles synthesis.

In order to minimize the possible discrepancies during each syntheses, it was only used and characterized the samples that reached the settled temperature before the defined maximum pressure. For all samples where the opposite occurred, it were discarded and a new attempt for synthesis was made.

The obtained samples were characterized with XRD, SEM and with a spectrometer UV-Vis-NIR for structural, size and shape and optical information, respectively.

4.2.1 XRD characterization

The normalized diffractograms for each sample are shown in figure 4.18.

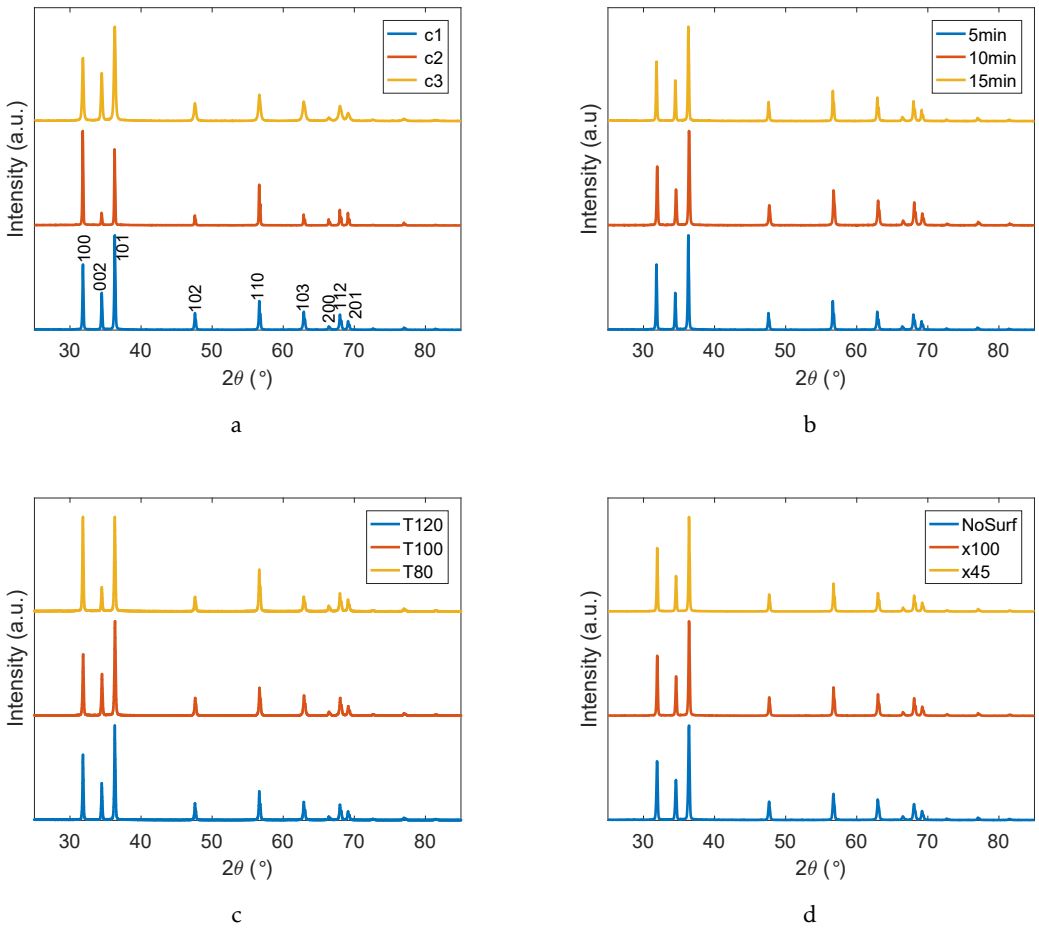

Figure 4.18: Normalized diffractograms of the synthesized ZnO nanoparticles. a) For different concentrations b) For different synthesis times c) For different synthesis temperatures d) For different surfactants.

Independently of the synthesis parameters, all diffractograms show the same peaks, which are indexed according to the hexagonal phase of ZnO. No other impurities peaks appeared on the diffractogram, which reveals a pure crystalline nature of the ZnO samples.

The ratio of peak intensity is not constant for different diffractograms. One possible explanation for this phenomenon is the random orientation and quantity of the dried ZnO nanoparticles (in powder form), such that some measurements have a more predominant orientation then others making the peaks intensity different for different diffractograms.

4.2.2 Optical characterization

Figure 4.19a shows the reflectance spectrum for the sample c1 as a function of the wavelength λ from 200 to 800 nm. All the other samples exhibited a similar profile and therefore only this reflectance spectrum is presented in this report.

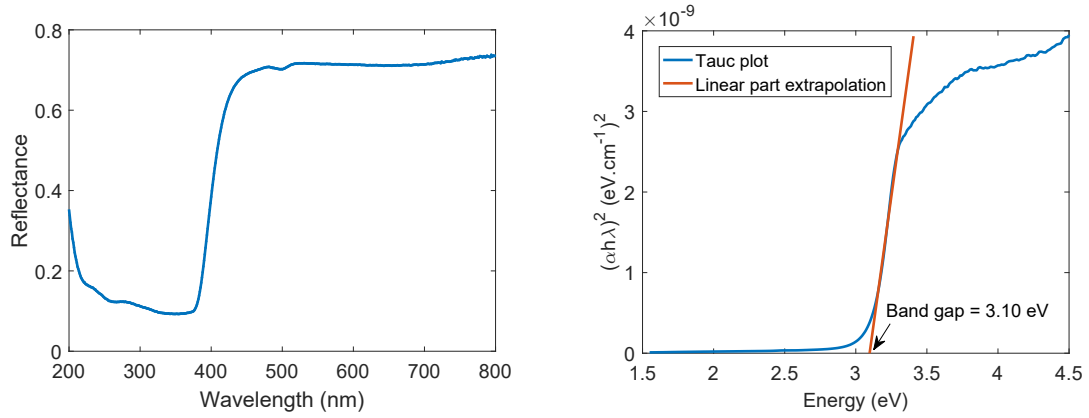

a b

Figure 4.19: Optical characterization for sample A a) Reflectance spectrum of sample A b) Tauc plot and extrapolation of the linear part for band gap calculation.

On the visible region, between 400 and 700 nm, there is a continuous reflectance of over 70%. At a wavelength of around 400 nm, which corresponds to the energy of the forbidden gap, a sharp transition is observed, where the reflectance percentage drops to 10 %.

The band gap was computed using the Tauc relation, explained in 3.2.2, where it was found the linear region of Tauc's plot through the maximum of its differential and then extrapolated until the linear part met the abscissa, (figure 4.19b). Table 4.5 resumes the band gaps computed for all synthesized ZnO samples.

Table 4.5: Values of the band gap computed for all synthesized ZnO samples.

Concentration solution A		
c1	c2	c3
3.06 eV	3.10 eV	3.08 eV
Surfactant		
NoSurf	x45	x100
3.11 eV	3.11 eV	3.10 eV
Synthesis Time		
5min	10min	15min
3.10 eV	3.12 eV	3.12 eV
Synthesis Temperature		
T80	T100	T120
3.08 eV	3.10 eV	3.10 eV

All samples displayed a band gap with energy values between 3.06 and 3.12 eV which,

according to the literature, meets expected the optical band gap of zinc oxide single crystals at room temperature [69].

However, little or no variation on the band gap has been observed as function of the synthesis parameters, which suggests no significant influence of the synthesis parameters on this physical quantity. Thereby, the optical characterization revealed to be an inconclusive parameter for the choice of the ideal conditions for the ZnO nanoparticles synthesis.

4.2.3 SEM and EDS characterization

The characterization by SEM aims to observe in more detail the morphology and size of the synthesized ZnO nanoparticles. Because no significant dependence on the parameters was extracted from XRD and optical characterization, these were optimized mainly by the analysis of SEM results, by searching for the highest surface/volume ratio in the observed nanoparticles. Table 4.6 shows the SEM images of all the synthesized ZnO samples.

In approximately all tests, the nanoparticles exhibit flower-like structures composed of sharp and hexagonal nanorods with tapered tips.

The results show that time and temperature are the parameters which most affect the morphology of the nanostructures. Longer times and higher temperatures yielded a better definition of the flower-like structures, with longer and thinner rods. Therefore, the longest synthesis time (15 minutes) and the highest temperature (120 °C) were selected as the optimized values for these parameters.

Opposite to what has been reported in literature, the presence of surfactants in the solution did not evidence a great impact on the morphology of the nanoparticles. In previous reports [70], surfactants should render the synthesized ZnO particles, producing narrower average width and a smaller aspect ratio. In the measurements here performed, it was not possible to directly observe such consequences, neither a significant difference between the surfactants. Therefore, the selection of the condition to be used in the optimized synthesis was derived taking into account the literature reports, where the use of surfactants is frequent, and secondly the homogeneity of the nanoparticles observed. As a result, the surfactant Trinton X-45 was selected for presenting a higher homogeneity in the size and volume ratio of the rods.

Regarding the concentration of solution A, the solution with the lowest concentration, c1, revealed the smallest ZnO nanoparticles. Between concentration c2 and c3, the difference was not clear. However, concentration c1 was the one chosen for the optimized synthesis because it is the concentration used in the paper on which this work was based in and because SEM images indicate higher homogeneity in the size and volume ratio of the rods.

Overall, the conditions chosen for the final ZnO synthesis, which were then used in the ultraviolet radiation sensor were:

- *Solution A* - c2 with 0.5 M of zinc acetate and 8 M of sodium hydroxide

Table 4.6: SEM images of all synthesized ZnO samples.

Concentration solution A		
c1	c2	c3
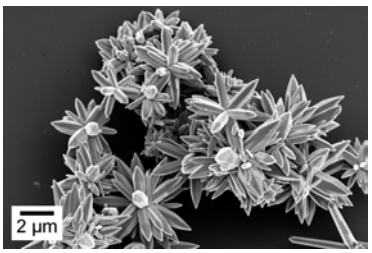	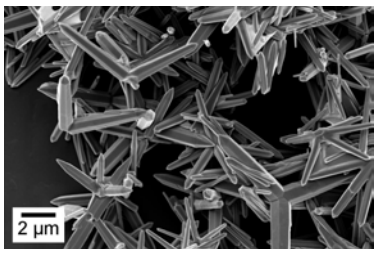	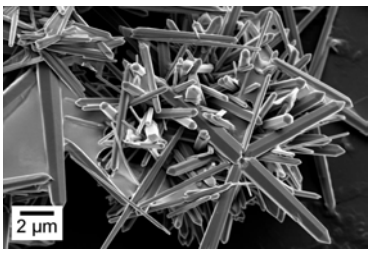
Surfactant		
NoSurf	x45	x100
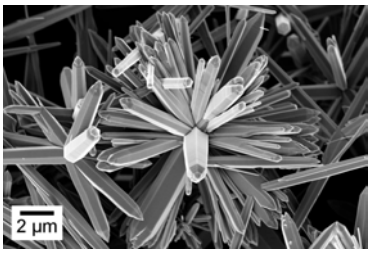	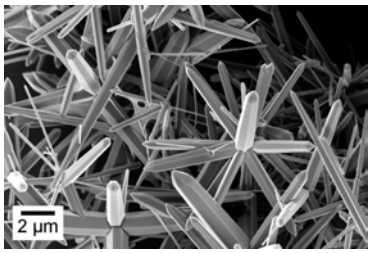	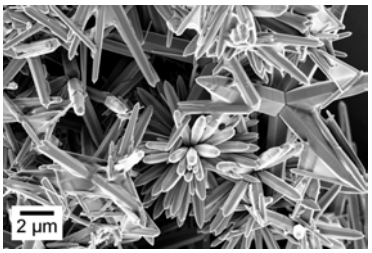
Synthesis Time		
5 min	10 min	15 min
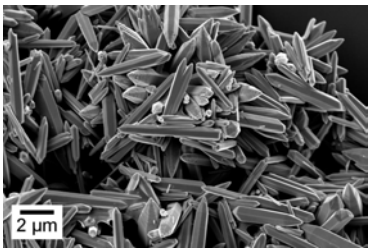	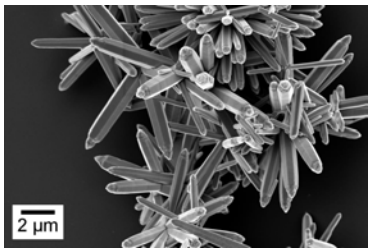	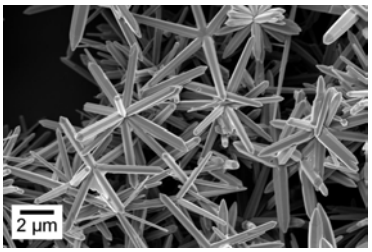
Synthesis Temperature		
80 C	100 C	120 C
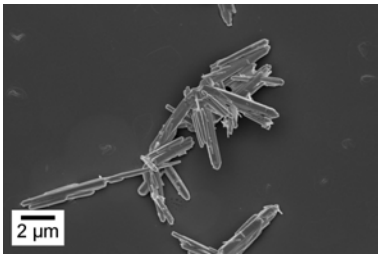	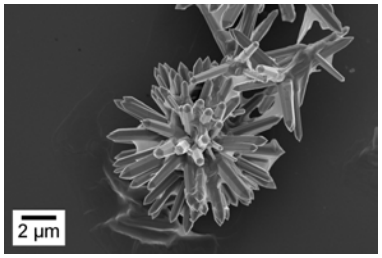	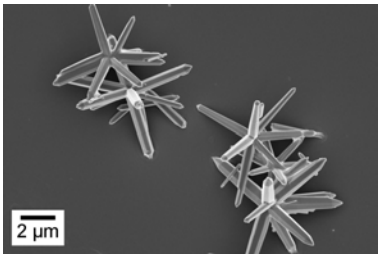

- *Solution B* - surfactant Triton X-45
- *Microwave exposure time* - 15 minutes
- *Microwave temperature* - 120 °C

In order to consolidate the conclusions obtained by SEM images and X-ray diffraction and to confirm that the flower-like structures are in fact the synthesized ZnO particles, an elementar analysis was performed by EDS to identify the chemical elements present in

the samples. Figure 4.20a shows the SEM image of the region in which the EDS analysis was carried out and figure 4.20b, the cumulative spectrum of the EDS analysis.

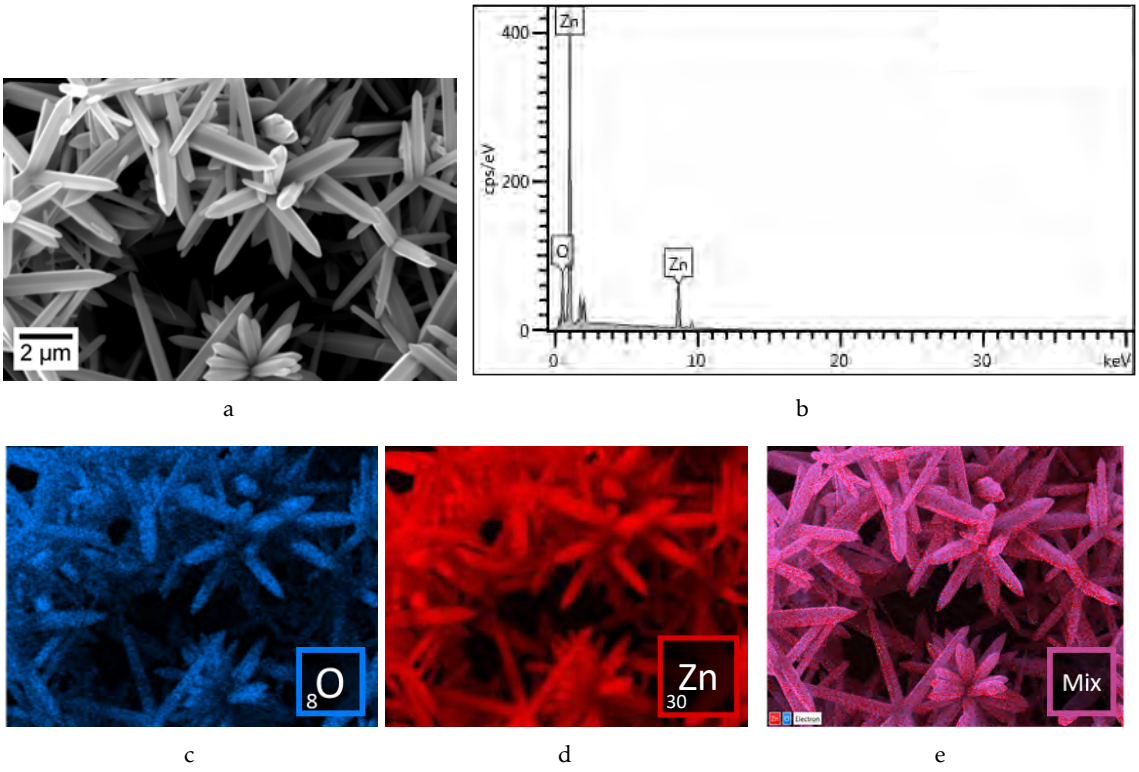

a b

c d e

Figure 4.20: EDS analysis of the sample with a synthesis time of 15 min a) SEM image of the region in which the EDS analysis was carried out, b) Cumulative spectrum of the EDS analysis, c,d,e) EDS mappings of oxygen, zinc and both elements respectively. The images were artificially colored to simplify the reading

In the EDS spectrum, the peaks corresponding to oxygen and zinc can be observed which validates the synthesis of zinc oxide occurrence.

EDS analysis was then used to map the abundance of the three elements in the sample. The maps are obtained by scanning the sample with the electron beam and binning the detected EDS spectra to the regions corresponding to characteristic peaks of each element, such that the abundance of a certain element in each pixel is encoded in its brightness. Figures 4.20c, 4.20d and 4.20e show the distribution maps of the two main constituents of ZnO and the sum of the two, respectively.

4.2.4 Optimized ZnO synthesis

With the optimized parameters chosen through the SEM characterization, a new synthesis was carried out and characterized for later use in the UV sensors.

Figure 4.21b presents SEM images taken from the optimized ZnO synthesis. These revealed flower-like structures composed of sharp and hexagonal nanorods with tapered tips, with a proximate length of 5.2 μm and 0.6 μm thick.

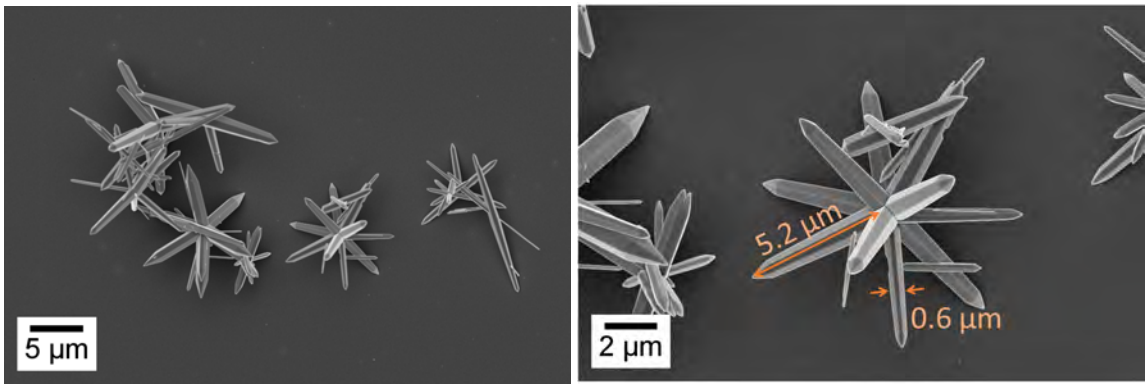

a b

Figure 4.21: SEM images of the optimized ZnO nanoparticles.

A new reflectance spectrum was also obtained in order to determine the band gap of the optimized ZnO nanoparticles, figure 4.23a. The Tauc plot corresponding to the reflectance spectrum is shown in figure 4.23b, together with an extrapolation of the linear part, whose intersection with the x axis corresponds to the band gap value. In this case, a band gap of 3.12 eV was determined, which corresponded to the maximum value obtained from all the syntheses made.

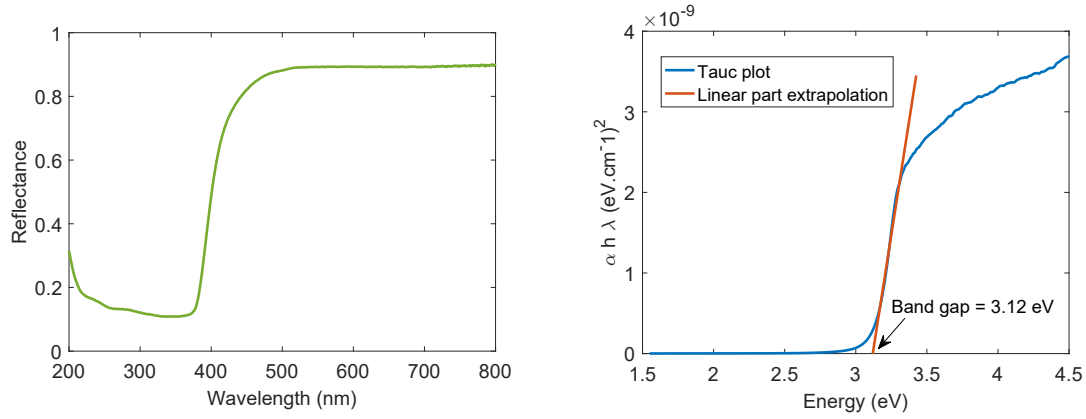

a b

Figure 4.22: Optical characterization for the optimized ZnO nanoparticles a) Reflectance spectrum b) Tauc plot and extrapolation of the linear part for band gap calculation.

4.3 UV sensor

4.3.1 Custom UV sensor

The production of UV sensors was the final part of this work and consisted in the combination of LIG electrodes produced and optimized in the section 4.1, with the ZnO nanoparticles synthesized by microwave irradiation, section 4.2.

The sensors were implemented by drop casting a dispersion of ZnO particles over interdigital electrodes build by LIG, after 15 minutes of UV light treatment to enhance its hydrophilicity. The effect of this treatment over both polymers (PI and PEI) before and after the UV treatment was evaluated by means of contact angle measurements. The results are shown in table 4.7.

Table 4.7: Contact angle measurements before and after UV treatment.

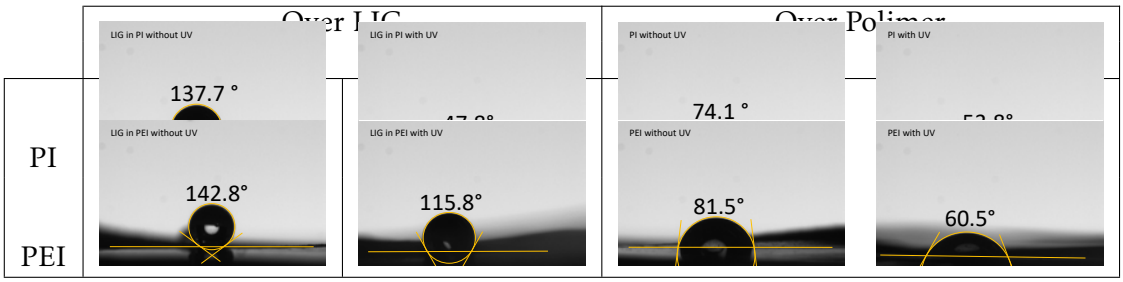

A decrease in the contact angles was observed after the UV treatment, which demonstrates a more hydrophilic substrate, which facilitates the uniform spread of the nanoparticles (figure 4.23).

Figure 4.23: UV treatment result. a) Photograph of a ZnO nanoparticles dispersion on top of an interdigital electrode made by LIG in PI before the 15 minutes of UV treatment. b)Photograph of a ZnO nanoparticles dispersion on top of an identical interdigital electrode after the UV treatment.

Once a uniform distribution of the nanoparticles was obtained, the sensors were characterized by measuring the current over time while applying a constant bias voltage of 1.0 V and cyclically exposing them to ultraviolet light.

Firstly, the influence of the geometry of interdigital electrodes on the responsivity of UV sensors was tested by laser-printing the designed electrodes in PI shown in table 4.8, using the selected ZnO nanoparticles and finally characterizing their response to UV exposure. The time-dependent results are shown in figure 4.24.

In the four tested sensors, the electrical current increased when exposed to UV radiation, therefore demonstrating sensitivity of the devices to radiation and the success in the implementation of a fully custom-built sensor.

Table 4.8: The four different interdigital geometries tested as UV sensor and the respective characteristics, detection area (in cm^2), number of contacts, width of each contact and the gap between contacts.

Design A	Design B	Design C	Design D
		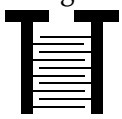	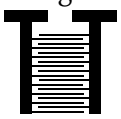
Detection area - 1.10 Contacts - 8 Width - 0.4 mm gap - 1 mm	Detection area - 0.95 Contacts - 8 Width - 0.2 mm gap - 1 mm	Detection area - 1.21 Contacts - 10 Widths - 0.2 mm gap - 1 mm	Detection area - 1.32 Contacts - 18 Width - 0.2 mm gap - 0.5 mm

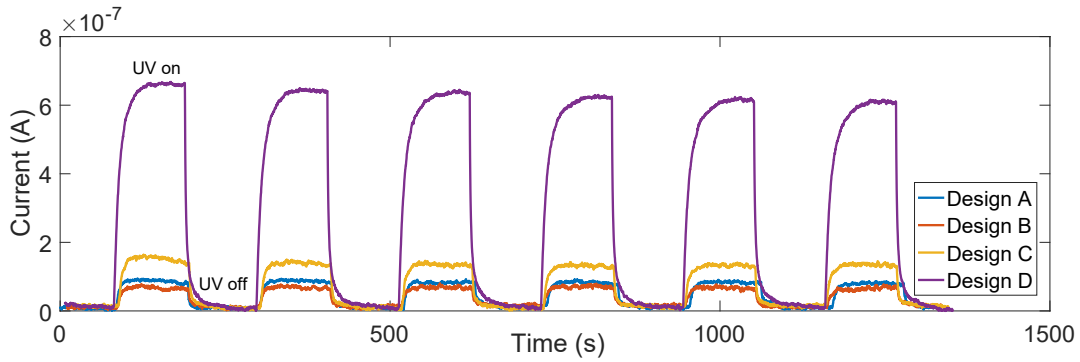

Figure 4.24: Photocurrent curves of the UV sensors at 1.0 V bias for the four interdigital geometries.

Interestingly, the different geometries exhibited a considerable influence in the responsivity of the sensors. The efficiency of an electrode depends on two main factors: (i) the detection area, the higher the area the more UV radiation is collected and (ii) the resistance of the interdigital electrodes. The geometry used for the sensors can be visualized as several resistors in parallel (figure 4.25a), so that the smaller the resistance, the larger the output current is. Thus, in order to increase the efficiency of the UV sensors, it is necessary to increase the detection area and reduce the resistance. The latter is influenced by the electrodes area, the number of contacts ($1/R = \sum 1/R$) and the gap between contacts (figure 4.25b).

From design A to B, it was intended to study the effect of the electrodes resistance by reducing the width of the interdigital lines. Design B outputted a lower responsivity (6.84 nA/W) than that of design A (8.96 nA/W). This effect can be explained by the low resistance of the electrodes relative to the gap regions. Effectively, in spite of reducing the resistance of the electrodes, the difference was rather small and the overall resistance of the device was kept approximately constant. On the other hand, lowering the thickness of the lines also lowered the detection area, whose effect was more prominent than the change of resistance and therefore the output current decreased.

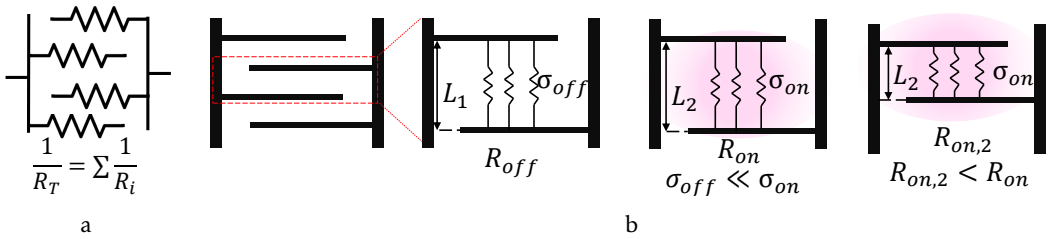

Figure 4.25: Representation of interdigital geometry a) Parallelism of an interdigital circuit with several resistors in parallel. b) Effect of the UV light and the gap between electrodes in the total resistance of a circuit.

From geometry B to C, the detection area was increased by increasing the number of contacts, which reduced the total parallel resistance. This produced an increase in the responsivity from 7 nA/W to 15 nA/W. In design D the total parallel resistance was further decreased by increasing the number of contacts and reducing the gap (the most resistive element of the sensor). This produced an increase in the value of responsivity up to 92 nA/W.

The response time of the sensors remained approximately constant for all geometries. However, the recovery time showed a progressive decrease from design A to D. Table 4.9 summarizes the parameters taken from the characterized sensors.

Table 4.9: Characteristics of the four characterized sensors with different geometries.

	Design A	Design B	Design C	Design D
I_{ph} - I_{dark} (nA)	72	55	117	737
Responsivity (nA/W)	8.9	6.8	14.6	92.1
Response time (s)	12.8	12.3	9.0	12.3
Recovery time (s)	11.5	8.8	5.8	5.5

Once obtained the geometry that resulted on a higher responsivity, a new sensor with the same design was developed with LIG electrodes over PEI and posteriorly characterized. Figure 4.26 shows the time-resolved photocurrent of the UV sensors built both over PI and PEI.

The large discrepancy of responsivity between the two sensors is readily apparent by the order of magnitude difference in the scales of the two plots. While the photocurrent gain (I_{ph}-I_{dark}) of the sensor with LIG in PI was determined to be around 700 nA, for PI, it was determined to be only of 18 nA. This can be explained by the much higher sheet resistance of the LIG in PEI than in PI, which consequently results in a much larger resistance of the interdigital electrode in PEI and a decrease in output current.

The response of the final sensors was then evaluated under strain, by performing electrical characterization of substrates pressed over molds with a curvature radius of 45, 25 and 15 cm. The resulting photocurrents are shown in figure 4.27a for the sensors on PI and in figure 4.27b for the sensors on PEI.

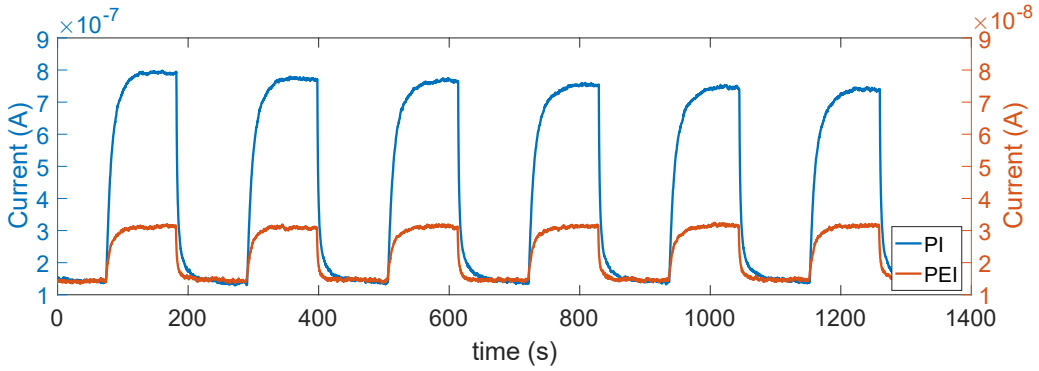

Figure 4.26: Photocurrent curves of the UV sensors at 1 V bias with geometry D developed over PI and PEI.

Table 4.10: Characteristics of the optimized PI sensor while working under deformation with curvature radius of 45, 25 and 15 cm.

	R45	R25	R15
I_{ph}-I_{dark}	273.0	261.0	175.0
Responsivity (nA/W)	34.1	32.6	21.9
Response time (s)	26.3	17.0	5.5
Recovery time (s)	5.3	5.0	16.3

For the sensor developed over PI, figure 4.27a shows a decrease of the responsivity for smaller bending radius and consequently higher strains. This can be explained both by the device resistance increment when stretched due to the size-increase of the conductors, or by the alteration of the light interaction with the sensor, which may be less efficient for larger angular scattering.

When stretching the device it becomes thinner and longer, increasing the interstitial spacing between the nanoparticles and the remaining conducting elements. In addition, the stretching can also result in the blockage of conductive electron pathways or forcing them to travel in more sinuous paths [25]. These effects increase the electrical resistance of the devices and therefore higher strains yield more resistive and less responsive sensors. Also, the interaction of light with the sensors changes with its deformation By decreasing the curvature radius, the light coupling with normal surface decreases and the angular dispersion increases, this leads to a loss of light absorption and thereby of the sensor responsivity.

Table 4.10 summarizes the parameters taken from sensors characterized under strain.

For the sensor developed over PEI (figure 4.27b), no change in responsiveness is observed for the different curvatures radius due to the poor measured signal and lowe signal/noise ratio. Thus, a possible difference in the responsivity of the sensor from the three curvature radius may be camouflaged in the background noise in such a way that no differences are visible.

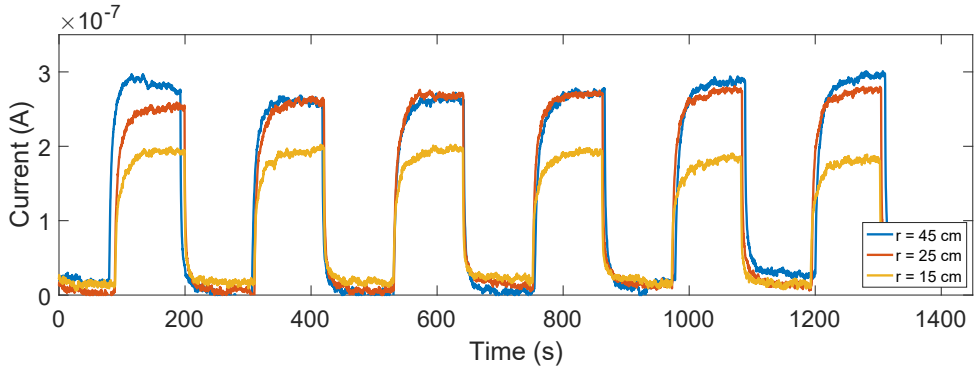

a

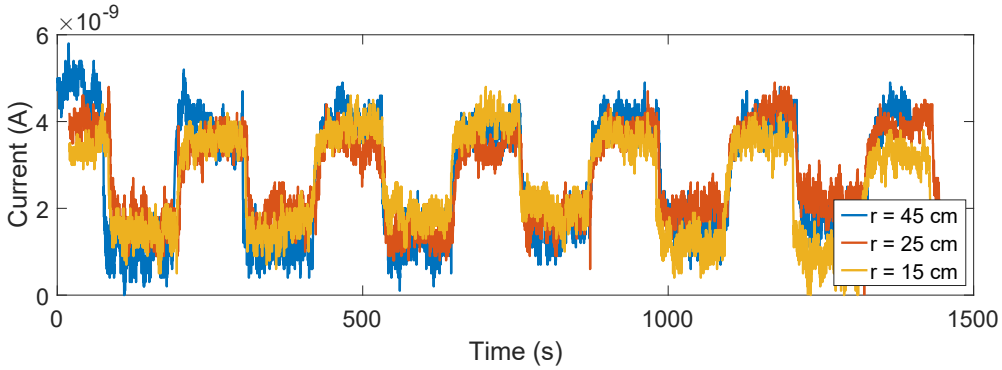

b

Figure 4.27: Flexibility test for a) PI UV sensor and for b) PEI UV sensor.

In order to analyze the stability of the UV sensor in long-term irradiation cycle with UV light, the UV sensor developed in PI was characterized during a total of ten hours, where it was subjected to 150 irradiation cycles of approximately 4 minutes (figure 4.28).

Throughout the characterization time, the sensor always reacted to the ultraviolet radiation. In fact, the responsivity has increased over time until stabilization.

Noting that UV treatment was used in the sensor preparation for modifying the adhesion properties of the electrodes to the ZnO nanoparticles, it is possible for long exposure to UV light to promote further enhancement of the sensor responsitivity.

Lastly, it was performed a cost-analysis of the materials used in the development of the sensors (table 4.11), where it has been calculated a cost of approximately 0.26 and 0.15 € per unit for the PI and PEI sensor, respectively. This analysis did not take into account the electricity nor equipment-wear costs (commercial CO_2 laser, microwave and the UV light for the hydrophilicity treatment).

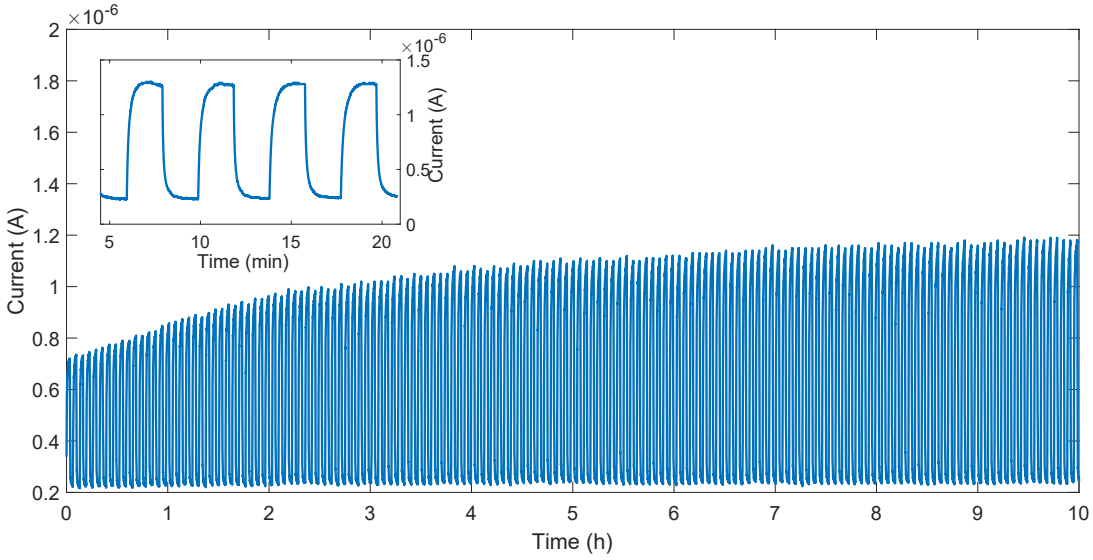

Figure 4.28: Photocurrent curves of the PI sensor at 1 V bias measured during ten hours of constant operation.

Table 4.11: Cost analysis of the PI and PEI developed UV sensors.

	Material	Quantity	Price/Quantity	Price/Sensor	
ZnO production	Zinc acetate	0.038 g	1.5 €/g	0.038 €	0.118 €
	Sodium hydroxide	0.080 g	0.80 €/g	0.064 €	
	Trinton X-45	0.0125 mL	0.128 €/mL	0.016 €	
Substrate	PI	4 cm^2	0.034 €/cm^2	0.139 €	
	PEI	4 cm^2	0.008 €/cm^2	0.032 €	
		Integrated cost	**PI sensor**	**0.257 €**	
			PEI sensor	**0.150 €**	

4.3.2 Custom versus commercial compounds of the UV sensors

The developed UV sensors were also compared with similar sensors built using commercial components. In this case, the production and characterization of (i) a sensor with carbon-ink electrodes over PI with the custom ZnO nanoparticles dispersion on top (ii) a sensor with LIG electrodes in PI with a dispersion of commercial ZnO nanoparticles were performed. The results are shown in figure 4.29.

As expected, in the interdigital electrodes without the nanoparticles dispersion, no current change was visible upon UV irradiation, which confirms the role of the ZnO nanoparticles as fundamental part on the UV detection.

Both sensors with commercial components exhibited higher responsivities (859 nA/W for the carbon ink and 362 nA/W for the commercial ZnO) when compared to the sensors assembled with the custom electrodes and ZnO nanoparticles (92 nA/W for the LIG in PI and 2 nA/W for the PI). Table 4.12 summarizes all the parameters taken from the characterization of the sensors with commercial components and of the customized

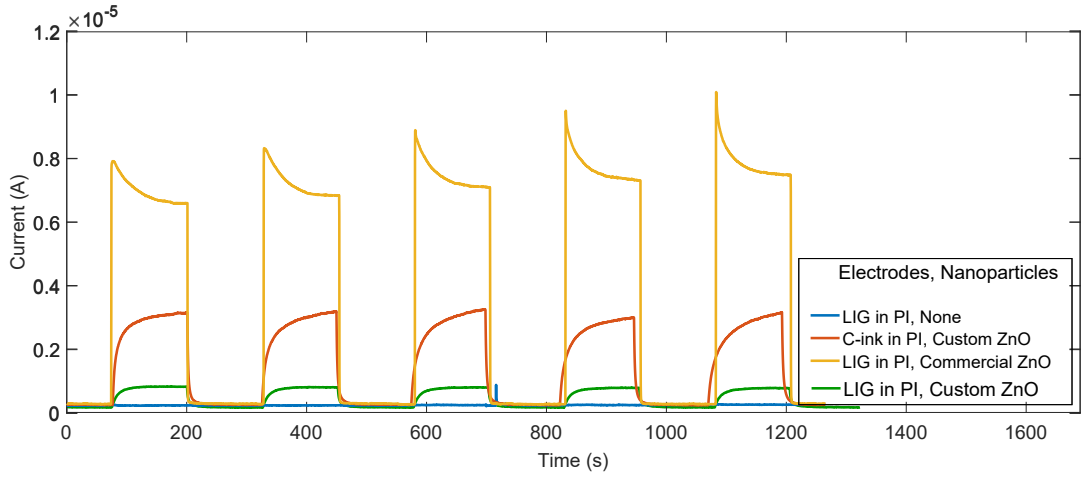

Figure 4.29: Comparison of the UV sensors with different commercial components (ZnO nanopowder and carbon ink).

sensors.

Table 4.12: Characteristics of the optimized PI and PEI sensors and comparison with sensors with commercial components.

Electrodes ZnO Nanoparticles	LIG in PI None	Carbon-ink Custom	LIG in PI Commercial	LIG in PI Custom	LIG in PEI Custom
I_{ph}-I_{dark} (nA)	0	2892.0	6872.0	737.0	15.8
Responsivity (nA/W)	-	362.0	859.0	92.0	2.0
Response time (s)	-	39.0	3.8	15.3	13.3
Recovery time (s)	-	5.8	5.5	5.5	5.3

The commercial carbon ink used revealed a sheet resistance of 15 $\Omega/square$, which is lower than the 20 $\Omega/square$ of the produced LIG electrodes. This results in a smaller sensor resistance, which increases its responsivity. However, the response time of the custom sensor is lower than the sensor with carbon paint Such an effect may be related to the high porosity of the LIG electrodes and therefore large surface area, which increases the sensitivity of the sensor to external factors, requiring thus a shorter response time.

On the other hand, the commercial nanoparticles have smaller size than the custom ones, with different morphology (figure 4.30). Particularly, this difference in particle size lead to an increase in the number of particles per sensor, for sensors using the same mass concentration, which increases its responsivity.

Certainly, the obtained sensors can still be further optimized, particularly, resourcing to commercially available and established materials. However, as proof of concept, the results demonstrated the possibility to obtain a perfectly functioning UV sensor using a fully custom-developed device and laser induced graphene.

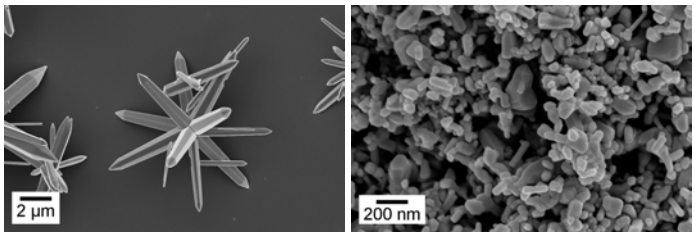

a b

Figure 4.30: SEM images of the ZnO nanoparticles tested as active layer in UV sensors a) Custom ZnO particles b) Commercial ZnO particles.

4.4 Production of electrodes in paper by laser direct writing

As an attempt to combine the production of electrodes through laser direct writing with other types of substrates, it was attempted to fabricate laser induced silver and copper electrodes on paper substrates. These type of substrate was chosen mainly due to its easy access, flexibility and its production cost, allowing thus the development of low-cost devices without the need of controlled atmospheres and high temperatures.

4.4.1 Laser induced silver electrodes

Regarding the silver electrodes produced by LDW in paper, a quick conductivity test was performed using a multimeter and it was observed that the two conditions with lowest speeds exhibited a minimum resistance on the order of hundred ohms. This test allowed concluding that lower speeds yield higher conductivity.

In order to improve these measurements, several lines with different laser speeds and powers were printed to measure the electrical resistance through IV curves. Also, silver ink was deposited at the edge of the lines to improve the contacts of the probes, (figure 4.31a).

Taking into account the oxidation problem, it was only possible to measure one IV curve for the line with 3.5 W of laser power and 0.38 m/s of scanning speed, figure 4.31b. The sheet resistance for the laser parameters described above was determined to be 54.47 $\Omega/square$, however this value can not be considered completely trustworthy. Given the rapid oxidation of the electrodes, out of all the printed lines of figure 4.31a, only one measurement could be performed, because all the others lines were damaged by the time of the measurement.

A laser induced silver electrode in paper substrate was analyzed in by SEM and EDS at the top view, (figure 4.32) and cross-section, (figure 4.33).

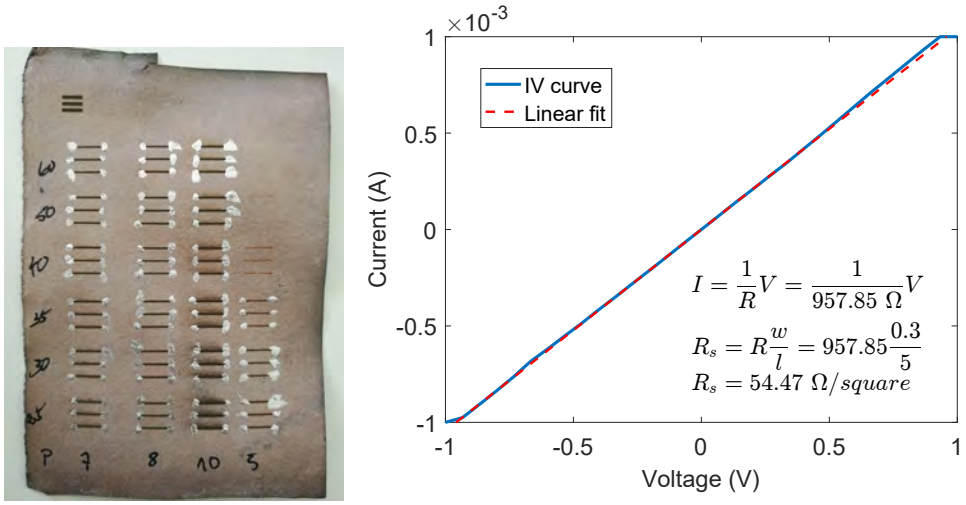

a b

Figure 4.31: Laser induced silver electrodes a) Photograph of the silver laser printed lines for further electrical characterization. b)IV curve for the line with 3.5 W of laser power and 0.38 m/s of scanning speed.

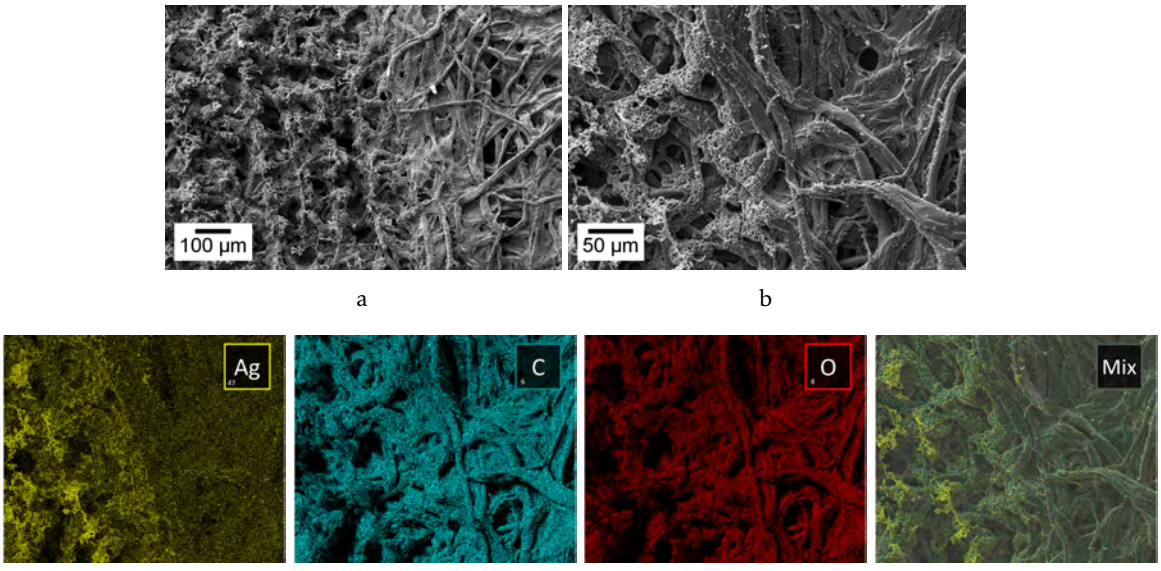

a b

c d e f

Figure 4.32: SEM images and EDS mappings of a laser induced silver electrode made in paper subtract. a,b) SEM images of the top view of the interface of the region where the laser focused and did not focus on the paper soaked with silver nitrate c,d,e)EDS silver, carbon and oxygen mapping of the region shown in b respectively f)EDS mapping of all the three elements.

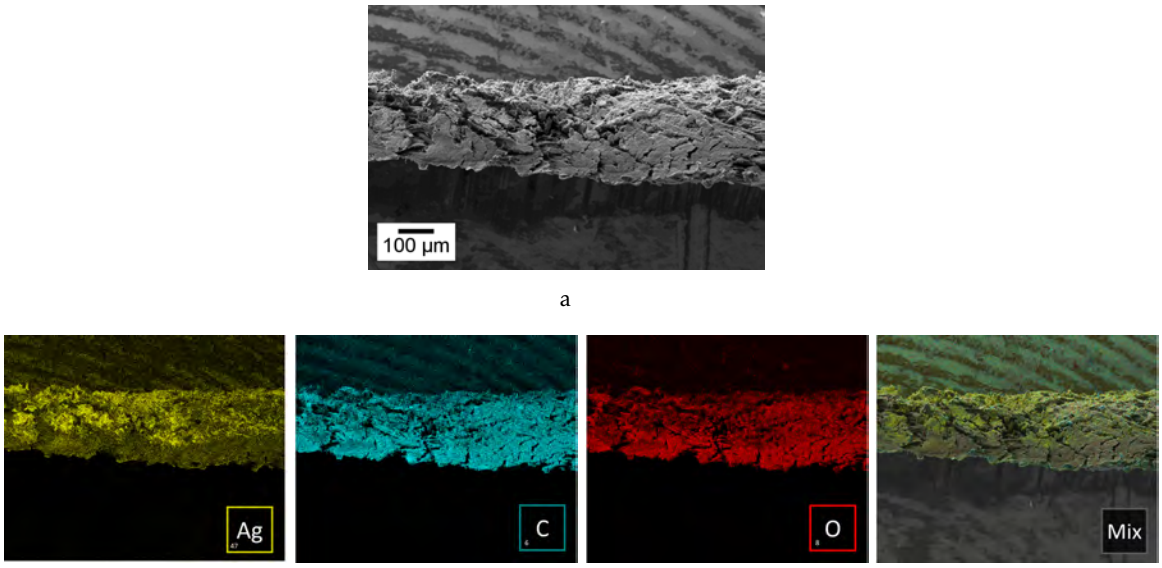

a b c d e

Figure 4.33: SEM images and EDS mappings of a cross sectioin of laser induced silver electrode made in paper subtract. a,b) SEM image of the cross section of laser induced silver in paper c,d,e)EDS silver, carbon and oxygen mapping of the region shown in a respectively f)EDS mapping of all the three elements.

The image 4.32 reveals significant changes in the paper morphology due to the exposure of the laser. When the laser passed on the paper impregnated with silver nitrate, a thermal effect occurred, leading to a decomposition of silver nitrate as described in equation 4.1.

$$2AgNO_3 \rightarrow 2Ag + O_2 + 2NO_2 \tag{4.1}$$

The EDS mappings revealed an increase in the silver concentration in the region where the laser passed and a slightly decrease on the oxygen concentration.

The cross-section images revealed, especially by the Ag EDS mapping, that the decomposition of silver nitrate occurs not only on the surface of the paper but up to approximately half of the paper thickness.

Overall, in spite of the rapid oxidation and strong photosensitivity, it has been proved that is possible to develop laser-induced silver electrodes on paper substrates. The technique is worth of further attention and optimization. In this work, it has been implemented in a simple LED circuit (figure 4.34) which takes into advantage the freedom of design provided by the laser-writing technique and the use of accessible and inexpensive materials such as paper.

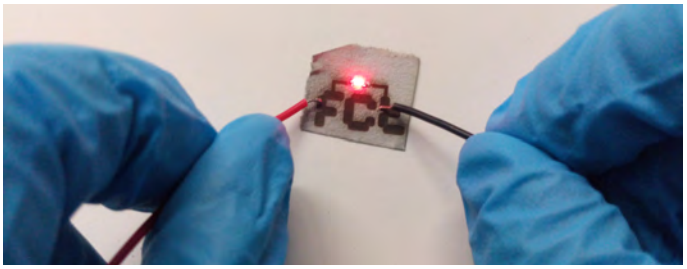

Figure 4.34: Proof of concept of the laser induced silver electrodes in paper subtracts - Photograph of a ON state LED connected to a silver electrode.

4.4.2 Laser induced copper electrodes

For the lase-induced copper electrodes, quick conductivity test was performed at the edges of the line using a multimeter. It was observed that the substrate became conductive in the place where the laser passed, presenting a resistance of 50 Ω.

However, the same issue found in the production of silver electrodes was found - the severe and rapid oxidation - but now with an even higher oxidation rate (in approximately 5 minutes the electrode stopped working), which prohibited any further characterization.

As an attempt of circumventing the severe oxidation problem, silver ink was brushed in the paper before placing the copper oxide solution. The objective was to take advantage of the electrode layer closed to the paper considering that only the surface oxidized (figure 4.35). Using this method, a slight increase in oxidation time was observed, however, it has not yet been sufficient for further studies.

Nevertheless, even with such inconvenient obstacle, it has been shown that it is possible to develop laser-induced copper electrodes on paper substrates. Is therefore required an optimization of these electrodes for production, encapsulation or other protections against the oxidation.

Figure 4.35: Photograph of a printed laser induced copper electrode with silver ink between the paper and the copper electrodes.

Chapter 5

Conclusions and Outlook

During this work, a UV sensor was developed using ZnO nanostructures the active layer, PI or PEI as substrates and LIG electrodes. In the presence of UV light the conductivity of the ZnO layer was observed to increase, giving rise to an increase of the current and thereby acting as a UV sensor. Overall, in this work, flexible and low-cost UV sensor was fully developed using a few fabrication steps and short production time.

A systematic study was performed, with the objective of determining the optimal parameters of a commercial CO_2 infrared laser-cutting equipment for the formation of LIG in two polymer surfaces. This study allowed the enhancement of the electrical properties of graphene stacked structures formed upon laser irradiation.

A strong influence of the laser parameters was observed on the LIG properties. Lower laser power yielded smaller widths and thicknesses, higher surface homogeneity and more compact films. Furthermore, the sheet resistance was observed to reach minimum values for lower laser powers and speed. From the two evaluated polymers, PI enabled formation of LIG with lower sheet resistances (20.91 $\Omega/square$) for a laser power of 8.50 W and speed of 0.14 m/s. On the other hand, LIG formed on PEI displayed a sheet resistance of 158.70 $\Omega/square$ for laser power of 3 W and speed 0.1 m/s.

The ZnO nanoparticles were synthesized through a microwave assisted hydrothermal method, which allowed a fast synthesis time, a low energetic cost and a precise control and uniform energy distribution, when compared with the conventional heating methods. The influence of several factors on the ZnO nanoparticles synthesis was evaluated. Namely, concentration of intermediate solutions, usage of surfactants, microwave-assisted synthesis time and temperature.

Nearly all evaluated conditions resulted in the formation of flower-like structures, composed of sharp and hexagonal nanorod with tapered tips. Longer synthesis times and higher temperatures lead to the formation of longer and thinner nanorods, which

increased the nanoparticles surface area and thereby the efficiency in detecting UV light, when applied in the sensors. Surfactant tests revealed that Trinton X-45 presented higher homogeneity in size and volume of the nanorods. Several characterization techniques were used to determine an optimal concentration of zinc acetate of 0.5 M and a concentration of NaOH of 8 M.

The final UV sensors were implemented by drop-casting the ZnO nanoparticles onto the optimized LIG electrodes, printed with an interdigital geometry. A study of the sensor responsivity as function of the interdigital electrode geometries allowed concluding that higher detection area, higher number of contacts and a smaller gap between the contacts maximize the sensor responsivity. Particularly, a responsitivity of 92 nA/W was obtained for PI and 2 nA/W for PEI, using a voltage of 1.0 V for both subtracts. Additionally, the PI sensor revealed a stronger suitability for working under strain and remarkable stability after several hours of continuous operation.

Moreover, laser-induced silver and copper electrodes were produced on paper subtracts. The products showed promising yet preliminary results, which may hold great interest in future research.

Having now optimized the fabrication parameters for stable and reproducible sensors, new applications for the flexible LIG electrodes, for instance deformation sensors, transistors, diagnostic-tests or solar cells are yet to be explored.

Regarding the zinc oxide nanoparticles a more detailed study on the importance of the concentration of the solution or the effect of the surfactant in the nanoparticles synthesis can be performed. On the other hand, the UV sensors can be further characterized for example the effect that the surrounding atmosphere might have in the UV sensors response.

Bibliography

[1] J. A. Rogers, T. Someya, and Y. Huang. "Materials and Mechanics for Stretchable Electronics." In: *Science* 327 (210), pp. 1603–1607. DOI: 10.1126/science.1182383.

[2] C. D. Dimitrakopoulos and D. J. Mascaro. "Organic thin-film transistors: A review of recent advances." In: *IBM Journal of Research and Development* 45.1 (2001), pp. 11–27. DOI: 10.1147/rd.451.0011.

[3] Q. H. Wang, K. Kalantar-Zadeh, A. Kis, J. N. Coleman, and M. S. Strano. "Electronics and optoelectronics of two-dimensional transition metal dichalcogenides." In: *Nature Nanotechnology* 7.11 (2012), pp. 699–712. DOI: 10.1038/nnano.2012.193.

[4] D. Tobjörk and R. Österbacka. "Paper electronics." In: *Advanced Materials* 23.17 (2011), pp. 1935–1961. DOI: 10.1002/adma.201004692.

[5] D. Marculescu, R. Marculescu, N. H. Zamora, P. Stanley-Marbell, P. K. Khosla, S. Park, S. Jayaraman, S. Jung, C. Lauterbach, W. Weber, T. Kirstein, D. Cottet, J. Grzyb, G. Tröster, M. Jones, T. Martin, and Z. Nakad. "Electronic textiles: A platform for pervasive computing." In: *Proceedings of the IEEE* 91.12 (2003), pp. 1995–2016. DOI: 10.1109/JPROC.2003.819612.

[6] S. Y. Kim, S. Park, H. W. Park, D. H. Park, Y. Jeong, and D. H. Kim. "Highly Sensitive and Multimodal All-Carbon Skin Sensors Capable of Simultaneously Detecting Tactile and Biological Stimuli." In: *Advanced Materials* 27.28 (2015), pp. 4178–4185. DOI: 10.1002/adma.201501408.

[7] C.-J. W. Babak Parviz. *Smart surgical glove*. 2014. URL: https://www.google.com/patents/US9402582.

[8] T. Someya. *Stretchable Electronics*. Ed. by P. T. Someya. Wiley-VCH Verlag, 2013, pp. 1–464. ISBN: 9783527326471.

[9] D.-m. Sun, M. Y. Timmermans, Y. Tian, A. G. Nasibulin, E. I. Kauppinen, S. Kishimoto, T. Mizutani, and Y. Ohno. "Flexible high-performance carbon nanotube integrated circuits." In: *Nature Nanotechnology* 6.3 (2011), pp. 156–161. DOI: 10.1038/nnano.2011.1.

[10] *Artificial skin heralds smarter robots and invisible body sensors - iQ UK*. URL: https://iq.intel.co.uk/artificial-skin-heralds-smarter-robots-and-invisible-body-sensors/ (visited on 10/03/2017).

[11] B. D.-h. Kim and J. A. Rogers. "Stretchable Electronics : Materials Strategies and Devices." In: *Advanced Materials* 20 (2008), pp. 4887–4892. DOI: 10.1002/adma.200801788.

[12] D. Mccoul, W. Hu, M. Gao, V. Mehta, and Q. Pei. "Recent Advances in Stretchable and Transparent Electronic Materials." In: *Advanced Materials* 2 (2016), pp. 1–51. DOI: 10.1002/aelm.201500407.

[13] T. H. E. Royal, S. Academy, and O. F. Sciences. *compiled by the Class for Physics of the Royal Swedish Academy of Sciences Graphene*. 2010.

[14] R. Vargas-bernal. "State-of-the-Art Electronic Devices Based on Graphene." In: *Nanoelectronics and Materials Development* (2016), pp. 1–15. DOI: 10.5772/64320.

[15] M. J. Allen, V. C. Tung, and R. B. Kaner. "Honeycomb carbon: A review of graphene." In: *Chemical Reviews* 110.1 (2010), pp. 132–145. DOI: 10.1021/cr900070d.

[16] W. Zhou, S. Bai, T. Hou, X. Shi, and A. Hu. "Laser direct writing of silver metal electrodes on transparent flexible substrates with high bonding strength." In: *Applied Materials and Interfaces* 8.37 (2016), pp. 24887–24892. DOI: 10.1021/acsami.6b07696.

[17] J. Lin, Z. Peng, Y. Liu, F. Ruiz-Zepeda, R. Ye, E. L. G. Samuel, M. J. Yacaman, B. I. Yakobson, and J. M. Tour. "Laser-induced porous graphene films from commercial polymers." In: *Nature Communications* 5.5714 (2014), pp. 1–8. DOI: 10.1038/ncomms6714.

[18] C. B. Arnold and A. Piqué. "L aser Direct-Write Processing." In: *MRS Bulletin* 32.January (2007), pp. 9–15.

[19] S. Bai, S. Zhang, W. Zhou, D. Ma, Y. Ma, P. Joshi, and A. Hu. "Laser-Assisted Reduction of Highly Conductive Circuits Based on Copper Nitrate for Flexible Printed Sensors." In: *Nano-Micro Letters* 9.42 (2017), pp. 1–13. DOI: 10.1007/s40820-017-0139-3.

[20] B. Kang, S. Han, J. Kim, S. Ko, and M. Yang. "One-Step Fabrication of Copper Electrode by Laser-Induced Direct Local Reduction and Agglomeration of Copper Oxide Nanoparticle." In: *Journal of Physical Chemistry C* 115 (2011), pp. 23664–23670. DOI: 10.1021/jp205281a.

[21] D. C. Christodouleas, F. C. Simeone, A. Tayi, S. Targ, J. C. Weaver, K. Jayaram, M. T. Fernández-Abedul, and G. M. Whitesides. "Fabrication of Paper-Templated Structures of Noble Metals." In: *Advanced Materials Technologies* 2 (2017), pp. 1–8. DOI: 10.1002/admt.201600229.

[22] M. F. El-Kady and R. B. Kaner. "Direct laser writing of graphene electronics." In: *ACS Nano* 8.9 (2014), pp. 8725–8729. DOI: 10.1021/nn504946k.

[23] R. Li, R Peng, K. D. Kihm, S. Bai, D. Bridges, U. Tumuluri, Z. Wu, T. Zhang, G. Compagnini, Z. Feng, and A. Hu. "High-rate in-plane micro-supercapacitors scribed onto photo paper using in-situ femtolaser-reduced graphene oxide/Au nanoparticle microelectrodes." In: *Energy Environ. Sci.* 9 (2016), pp. 1458–1467. DOI: 10.1039/C5EE03637B.

[24] R. Q. Ye, Z. W. Peng, T Wang, Y. N. Xu, J. B. Zhang, Y. L. Li, L. G. Nilewski, J Lin, and J. M. Tour. "In Situ Formation of Metal Oxide Nanocrystals Embedded in Laser-Induced Graphene." In: *ACS nano* 9 (2015), pp. 9244–9251. DOI: 10.1021/acsnano.5b04138.

[25] S. Luo, P. T. Hoang, and T. Liu. "Direct Laser Writing for Creating Porous Graphitic Structures and Their Use for Flexible and Highly Sensitive Sensor and Sensor Arrays." In: *Carbon* 96 (2015), pp. 522–531. DOI: 10.1016/j.carbon.2015.09.076.

[26] DUPONT™. *KAPTON® SUMMARY OF PROPERTIES*. 2017.

[27] J Davenas. "Influence of the temperature on the beam induced conductivity of polyimide." In: *Applied Surface Science* 43 (1989), pp. 218–223.

[28] M. Schumann, R. Sauerbrey, and M. C. Smayling. "Permanent increase of the electrical conductivity of polymers induced by ultraviolet laser radiation." In: *Applied Physics Letters* 58.4 (1991), pp. 428–430. DOI: 10.1063/1.104624.

[29] H. Phillips, D. Callahan, R. Sauerbrey, G. Szabo, and Z. Bor. "Direct Laser Ablation of Sub-100 nm Line Structures into Polyimide." In: *Applyed Physics A* 54 (1992), pp. 158–165. DOI: 10.1007/BF00323903.

[30] E. E. Ortelli, F Geiger, T Lippert, J Wei, and A Wokaun. "UV-Laser-Induced Decomposition of Kapton Studied by Infrared Spectroscopy." In: *Macromolecules* 33 (2000), pp. 5090–5097. DOI: 10.1021/ma000389a.

[31] J. Luo, F. R. Fan, T. Jiang, Z. Wang, W. Tang, C. Zhang, and M. Liu. "Integration of micro-supercapacitors with triboelectric nanogenerators for a flexible self-charging power unit." In: *Nano Research* 8.12 (2015), pp. 3934–3943. DOI: 10.1007/s12274-015-0894-8.

[32] J. Bin, B. Hsia, J.-h. Yoo, S. Hyun, C. Carraro, R. Maboudian, and C. P. Grigoropoulos. "Facile fabrication of flexible all solid-state micro-supercapacitor by direct laser writing of porous carbon in polyimide." In: *CARBON* 83 (2014), pp. 144–151. ISSN: 0008-6223. DOI: 10.1016/j.carbon.2014.11.017. URL: http://dx.doi.org/10.1016/j.carbon.2014.11.017.

[33] Z. Peng, J. Lin, R. Ye, E. L. G. Samuel, and J. M. Tour. "Flexible and stackable laser-induced graphene supercapacitors." In: *ACS Applied Materials and Interfaces* 7.5 (2015), pp. 3414–3419. DOI: 10.1021/am509065d.

[34] J. Cai, C. Lv, and A. Watanabe. "Cost-effective fabrication of high-performance flexible all-solid-state carbon micro-supercapacitors by blue-violet laser direct writing and further surface treatment." In: *J. Mater. Chem. A* 4.5 (2016), pp. 1671–1679. DOI: 10.1039/C5TA09450J.

[35] V. Strong, S. Dubin, M. F. El-Kady, A. Lech, Y. Wang, B. H. Weiller, and R. B. Kaner. "Patterning and electronic tuning of laser scribed graphene for flexible all-carbon devices." In: *ACS Nano* 6.2 (2012), pp. 1395–1403. DOI: 10.1021/nn204200w.

[36] F. Tehrani and B. Bavarian. "Facile and scalable disposable sensor based on laser engraved graphene for electrochemical detection of glucose." In: *Scientific Reports* 6.January (2016), pp. 1–10. DOI: 10.1038/srep27975.

[37] M. E. Lee and A. M. Armani. "Flexible UV Exposure Sensor Based on UV Responsive Polymer." In: *ACS Sensors* 1.10 (2016), pp. 1251–1255. DOI: 10.1021/acssensors.6b00491.

[38] L. Sang, M. Liao, and M. Sumiya. "A Comprehensive Review of Semiconductor Ultraviolet Photodetectors: From Thin Film to One-Dimensional Nanostructures." In: *Sensors* 13 (2013), pp. 10482–10518. DOI: 10.3390/s130810482.

[39] A. Pimentel, S. H. Ferreira, D. Nunes, T. Calmeiro, R. Martins, and E. Fortunato. "Microwave synthesized ZnO nanorod arrays for UV sensors: A seed layer annealing temperature study." In: *Materials* 9.4 (2016). DOI: 10.3390/ma9040299.

[40] K. K.-z. B. Fry. "Sensor Characteristics and Physical Effects." In: *Nanotechnology-Enabled Sensors*. Boston, MA: Springer US, 2008, pp. 13–62. DOI: 10.1007/978-0-387-68023-1_2.

[41] M. H. Mamat, M. I. Che Khalin, N. N. H. Nik Mohammad, Z. Khusaimi, N. D. Md Sin, S. S. Shariffudin, M. Mohamed Zahidi, and M. R. Mahmood. "Effects of annealing environments on the solution-grown, aligned aluminium-doped zinc oxide nanorod-array-based ultraviolet photoconductive sensor." In: *Journal of Nanomaterials* 2012 (2012), pp. 1–15. DOI: 10.1155/2012/189279.

[42] A. Pimentel. *Desenvolvimento de películas à base de ZnO, condutoras e resistivas para aplicação em electrónica transparente*. Tech. rep. 2006, p. 167. DOI: 10.1088/0022-3719/9/7/009.

[43] S. Masuda, K. Kitamura, Y. Okumura, S. Miyatake, H. Tabata, and T. Kawai. "Transparent thin film transistors using ZnO as an active channel layer and their electrical properties." In: *Journal of Applied Physics* 93.3 (2003), pp. 1624–1630. DOI: 10.1063/1.1534627.

[44] B. P. Rand, J. Genoe, P. Heremans, and J. Poortmans. "Solar Cells Utilizing Small Molecular Weight Organic Semiconductors." In: *Prog. Photovolt: Res. Appl.* 15.February 2013 (2007), pp. 659–676. DOI: 10.1002/pip.

[45] A Pimentel, D Nunes, P Duarte, J Rodrigues, F. M. Costa, T Monteiro, R Martins, and E Fortunato. "Synthesis of Long ZnO Nanorods under Microwave Irradiation or Conventional Heating." In: *Journal of P* 118 (2014), pp. 14629–14639. DOI: 10.1021/jp5027509.

[46] K. J. Chen, F. Y. Hung, S. J. Chang, and S. J. Young. "Optoelectronic characteristics of UV photodetector based on ZnO nanowire thin films." In: *Journal of Alloys and Compounds* 479 (2009), pp. 674–677. DOI: 10.1016/j.jallcom.2009.01.026.

[47] X. Zhang, J. Qin, Y. Xue, P. Yu, B. Zhang, L. Wang, and R. Liu. "Effect of aspect ratio and surface defects on the photocatalytic activity of ZnO nanorods." In: *Scientific Reports* 4 (2015), pp. 1–8. DOI: 10.1038/srep04596.

[48] A. Naveed, U. Haq, A. Nadhman, I. Ullah, G. Mustafa, M. Yasinzai, and I. Khan. "Synthesis Approaches of Zinc Oxide Nanoparticles : The Dilemma of Ecotoxicity." In: *Journal of Nanomaterials* 2017 (2017), pp. 1–14. DOI: 10.1155/2017/8510342.

[49] C. O. Kappe, D. Dallinger, and S. S. Murphree. *Practical Microwave Synthesis for Organic Chemists: Strategies, Instruments, and Protocols*. 2009, pp. 1–299. DOI: 10.1002/9783527623907.

[50] P. Zhu, J. Zhang, Z. Wu, and Z. Zhang. "2008 Microwave-Assisted Synthesis of Various ZnO Hierarchical Nanostructures : Effects of Heating Parameters of Microwave Oven." In: *Crystal Growth and Design* 8.9 (2008), pp. 3148–3153. DOI: 10.1021/cg0704504.

[51] M. Song. "The role of pH variation on the growth of zinc oxide nanostructures." In: *Applied Surface Science* 255.February (2009), pp. 4891–4896. DOI: 10.1016/j.apsusc.2008.12.037.

[52] M Razeghi and A Rogalski. "Semiconductor ultraviolet detectors." In: *Jour* 79.10 (1996), pp. 7433–7474.

[53] D. Cammi and C. Ronning. "Persistent Photoconductivity in ZnO Nanowires in Different Atmospheres." In: *Advances in Condensed Matter Physics* (2014), pp. 1–6. DOI: 10.1155/2014/184120.

[54] T. Zhai, X. Fang, M. Liao, X. Xu, H. Zeng, B. Yoshio, and D. Golberg. "A Comprehensive Review of One-Dimensional Metal-Oxide Nanostructure Photodetectors." In: *sensors* 9 (2009), pp. 6504–6529. DOI: 10.3390/s90806504.

[55] A. M. Takahashi, Yasutaka; Kanamori, Masaaki; Kondoh. "Photoconductivity of Ultrathin Zinc Oxide Film." In: *Japanese Journal of Applied Physics* 33 (1994), pp. 6611–6615. DOI: 10.1143/JJAP.33.6611.

[56] J. Powell. *CO2 Laser Cutting*. 2nd. Springer Berlin Heidelberg, 1998, p. 258. DOI: 10.1007/978-1-4471-1279-2.

[57] M. Csele. *Fundamentals of light sources and lasers*. Vol. 1. John Wiley and Sons, 2004, p. 344. ISBN: 9786468600. DOI: 10.1097/00024382-200205000-00022. URL: http://books.google.com/books?id=8Q003u9IfPYC{\&}pgis=1.

[58] E. Thostenson and T.-W. Chou. "Microwave processing: fundamentals and applications." In: *Composites Part A: Applied Science and Manufacturing* 30.9 (1999), pp. 1055–1071. DOI: 10.1016/S1359-835X(99)00020-2.

[59] H. Brittany. *Microwave synthesis: chemistry at the speed of light*. 2003. DOI: 10.5860/CHOICE.40-4619.

[60] E. G. Shafrin and W. A. Zisman. "Constitutive relations in the wetting of low energy surfaces and the theory of the retraction method of preparing monolayers." In: *The Journal of Physical Chemistry* 64.5 (1960), pp. 519–524. DOI: 10.1021/j100834a002.

[61] A. B. D. Cassie. "Contact angles." In: *Discussions of the Faraday Society* 3 (1948), p. 11. DOI: 10.1039/df9480300011.

[62] P. Prepelita, N. Stefan, C. Luculescu, F. Garoi, and R. Birjega. "Evolution of the properties of ZnO thin films subjected to heating treatments." In: *Thin Solid Films* 520.14 (2012), pp. 4689–4693. DOI: 10.1016/j.tsf.2011.10.168.

[63] R. Rusdi, A. A. Rahman, N. S. Mohamed, N. Kamarudin, and N. Kamarulzaman. "Preparation and band gap energies of ZnO nanotubes, nanorods and spherical nanostructures." In: *Powder Technology* 210.1 (2011), pp. 18–22. DOI: 10.1016/j.powtec.2011.02.005.

[64] R. Igreja and C. J. Dias. "Analytical evaluation of the interdigital electrodes capacitance for a multi-layered structure." In: 112 (2004), pp. 291–301. DOI: 10.1016/j.sna.2004.01.040.

[65] E Fortunato, N Correia, P Barquinha, L Pereira, G Gonçalves, and R Martins. "High-Performance Flexible Hybrid Field-Effect Transistors Based on Cellulose Fiber Paper (Paper Transistor) Outline." In: *Materials Science* 29.9 (2008), pp. 988–990. DOI: 10.1109/LED.2008.2001549.

[66] A. C. Ferrari, J. C. Meyer, V. Scardaci, C. Casiraghi, M. Lazzeri, F. Mauri, S. Piscanec, D. Jiang, K. S. Novoselov, S. Roth, and A. K. Geim. "Raman spectrum of graphene and graphene layers." In: *Physical Review Letters* 97.18 (2006), pp. 1–4. DOI: 10.1103/PhysRevLett.97.187401.

[67] H. W. Qiu, S. C. Xu, P. X. Chen, S. S. Gao, Z. Li, C. Zhang, S. Z. Jiang, M. Liu, H. S. Li, and D. J. Feng. "A novel surface-enhanced Raman spectroscopy substrate based on hybrid structure of monolayer graphene and Cu nanoparticles for adenosine detection." In: *Applied Surface Science* 332 (2015), pp. 614–619. DOI: 10.1016/j.apsusc.2015.01.231.

[68] S. A. El-Khodary, G. M. El-Enany, M. El-Okr, and M. Ibrahim. "Preparation and Characterization of Microwave Reduced Graphite Oxide for High-Performance Supercapacitors." In: *Electrochimica Acta* 150.October (2014), pp. 269–278. DOI: 10.1016/j.electacta.2014.10.134.

[69] V. Srikant and D. R. Clarke. "On the optical band gap of zinc oxide." In: *Journal of Applied Physics* 83.10 (1998), pp. 5447–5451. DOI: 10.1063/1.367375.

[70] H. Usui. "Influence of surfactant micelles on morphology and photoluminescence of zinc oxide nanorods prepared by one-step chemical synthesis in aqueous solution." In: *Journal of Physical Chemistry C* 111.26 (2007), pp. 9060–9065. DOI: 10.1021/jp071388o.